



Stressful crystal histories recorded around melt inclusions in volcanic quartz

Tyler Cadena¹ · Michael Manga¹ · Kenneth Befus² · Nobumichi Tamura³

Received: 25 October 2023 / Accepted: 19 March 2024 / Published online: 25 May 2024
© The Author(s) 2024

Abstract

Magma ascent and eruption are driven by a set of internally and externally generated stresses that act upon the magma. We present microstructural maps around melt inclusions in quartz crystals from six large rhyolitic eruptions using synchrotron Laue X-ray microdiffraction to quantify elastic residual strain and stress. We measure plastic strain using average diffraction peak width and lattice misorientation, highlighting dislocations and subgrain boundaries. Quartz crystals across studied magma systems preserve similar and relatively small magnitudes of elastic residual stress (mean 53–135 MPa, median 46–116 MPa) in comparison to the strength of quartz (~10 GPa). However, the distribution of strain in the lattice around inclusions varies between samples. We hypothesize that dislocation and twin systems may be established during compaction of crystal-rich magma, which affects the magnitude and distribution of preserved elastic strains. Given the lack of stress-free haloes around faceted inclusions, we conclude that most residual strain and stress was imparted after inclusion faceting. Fragmentation may be one of the final strain events that superimposes stresses of ~100 MPa across all studied crystals. Overall, volcanic quartz crystals preserve complex, overprinted deformation textures indicating that quartz crystals have prolonged deformation histories throughout storage, fragmentation, and eruption.

Keywords Residual stress · Plastic strain · Laue microdiffraction · Melt inclusions · Quartz · Fragmentation

Introduction

The dynamics of magma during storage, ascent, and eruption are driven by external and internal forces (Cassidy et al. 2018). Crystals present in the magma are witnesses of those forces. Similar to how crystals capture geochemical, temperature, and pressure conditions through their composition and trapped inclusions, they can also record some of the strains produced by forces they experience (e.g., Wheeler et al. 2001; Kendrick et al. 2017; Befus et al. 2019; Barbee et al. 2020). Those strains can arise from stresses imparted

by force chains between crystals in regions where magma accumulates, is stored, and then is mobilized (Cates et al. 1998; Bergantz et al. 2017). Crystals are further stressed as magma fragments during eruption. With potential signatures of multiple overprinted stress events, connecting recorded stresses in crystals to specific processes and eruption chronology can be ambiguous.

Strains in volcanic crystals can be measured with various techniques. Undulatory extinction observed under cross polars is the simplest method. Strain magnitude has been quantified by electron backscatter diffraction (EBSD). EBSD measurements have been useful for recording the stresses from storage, e.g., in melt-rich mush piles (Vinet et al. 2015; Wieser et al. 2020), to strain localization during extrusion (Wallace et al. 2019; Lavalloé and Kendrick 2022) and the brittle-ductile transition that accompanies fragmentation (Kendrick et al. 2017). Strains have also been measured and mapped more directly using X-ray microdiffraction (μ XRD), by comparing the lattice spacing and parameters of a stressed crystal to that of an ideal, non-stressed standard (Kunz et al. 2009; Tamura 2014; Vinet et al. 2015).

Communicated by Othmar Müntener.

✉ Tyler Cadena
tcadena@berkeley.edu

¹ Earth and Planetary Science, University of California, Berkeley, Berkeley, CA, USA

² Jackson School of Geosciences, University of Texas at Austin, Austin, TX, USA

³ Advanced Light Source, Lawrence Berkeley National Laboratory, Berkeley, CA, USA

To elucidate the magnitude and relative timing of strain events experienced and recorded by crystal cargo that eventually reaches Earth's surface in large explosive volcanic eruptions, we microstructurally characterized quartz crystals from six large-volume high-silica rhyolite eruptions using μ XRD. Throughout the magma system, growing crystals commonly entrap small (~ 10 – 100 μm) parcels of surrounding melt inside the crystal, that are then preserved as pressurized capsules of glass. We targeted our analyses to crystal domains surrounding these melt inclusions to exploit the relationship of melt inclusion entrapment and spontaneous inclusion faceting to show that most strain preserved in the crystals was imparted post-faceting (e.g., Gualda et al. 2012; Pamukcu et al. 2015; Boro et al. 2021). Crystals preserve a complex record of elastic and plastic strains that are overprinted and modulated by strain events throughout the lifetime of the crystal, including mush compaction, ascent, and fragmentation. Residual elastic stresses are on the order of ~ 100 MPa, a much lower magnitude than the strength of quartz (~ 10 GPa) (Goldsby et al. 2004; Broz et al. 2006; Whitney et al. 2007; Strozewski et al. 2021; Ceccato et al. 2022). We hypothesize this is a product of the unique spatiotemporal integration of strain and stress experienced by each crystal, impacted by the interplay of dislocation migration and lockup, and the presence of the inclusion on the surrounding crystal lattice.

Samples and Methods

Quartz crystals were manually extracted from gently crushed pumice clasts collected from pyroclastic deposits emplaced during large explosive eruptions of high-silica rhyolite (Table 1). Each crystal was examined under a petrographic microscope for melt inclusions that shared similar radii and position within the crystal. We targeted inclusions ~ 100 μm in diameter that were far from the edges of the host crystal. The host quartz crystals are 1–4 mm in diameter and range from anhedral and partially fractured to euhedral hexagonal bipyramids. Inclusions display varying amounts of faceting and bubbles. In some crystals, adjacent inclusions were chosen to sample different inclusion textures within the same crystal, including two with cracks not produced by sample preparation (Fig. 1). Crystals were mounted on glass slides with Crystalbond before being polished using progressively finer grits until the targeted inclusion was exposed on the flat polished surface.

All crystals were analyzed using synchrotron X-ray microdiffraction (μ XRD) at beamline 12.3.2 of the Advanced Light Source, Lawrence Berkeley National Laboratory, USA (Tamura et al. 2009; Tamura 2014). Diffraction patterns were collected with a DECTRIS Pilatus 1 M detector. A typical experiment analyzed an area of ~ 400 by 400 μm , using a spot size of ~ 1 μm^2 , a 5 - μm step, and 0.5 s exposure time. All samples were scanned using polychromatic X-rays (Laue diffraction). Data was processed in X-ray

Table 1 General descriptions of volcanic deposits from which quartz crystals were extracted for this study

Eruptive unit	Location	Deposit	Age (Ma)	Volume (km^3)	Crystallinity (%)	References
Bishop Tuff	Long Valley Caldera, CA, USA	Ignimbrite. Tableland lobe (Ig2E, mid)	0.7648 ± 0.0006	> 600	9.5–16.6	Andersen et al. (2017) Bailey et al. (1976) Pamukcu et al. (2012)
Bandelier Tuff	Valles Caldera, NM, USA	Fall pumice. Tsankawi Pumice Bed (upper)	1.256 ± 0.010	400	5	Waelkens et al. (2022) Phillips et al. (2007) Smith and Bailey (1966)
La Primavera	La Primavera Caldera, Jalisco, Mexico	Air-fall deposit. Giant Pumice Horizon	0.0864 ± 0.0051	0.15	1	Sourisseau et al. (2023) Mahood (1981)
Huckleberry Ridge Tuff	Island Park Caldera, Yellowstone, WY, USA	Fall deposit pumice	2.059 ± 0.004	~ 2450	~ 11 – 20	Swallow et al. (2019) Lanphere et al. (2002) Christiansen (2001)
Tuff of Bluff Point	Yellowstone Caldera, Yellowstone, WY, USA	Unwelded ignimbrite	0.1731 ± 0.005	50	6–12	Befus and Gardner (2016) Christiansen et al. (2007) Christiansen (2001)
Mesa Falls Tuff	Henry's Fork Caldera, Yellowstone, ID, USA	Fall deposit pumice	1.292 ± 0.005	280	20	Tollan et al. (2019) Rivera et al. (2016) Christiansen (2001)

Fig. 1 Photomicrographs of target melt inclusions in quartz crystals from the eruptions listed in Table 1. All scale bars are 100 μm . For samples with cracks (Bluff Point and Primavera), the cracks were found to be fully contained within the crystal before sample preparation began. The Bandelier, La Primavera, Huckleberry, and Bluff Point inclusions contain volumetrically small bubbles (< few vol.%). Bishop and La Primavera inclusions are clear glass whereas Huckleberry and Bluff Point inclusions are brown and contain incipient crystals. All inclusions are partially or fully faceted. The dark smudge on the lower side of the Primavera inclusion is polishing paste



Microdiffraction Analysis Software (XMAS) (Tamura 2014) and MATLAB package Crystal Calculating, Analyzing, and Mapping Program (XtalCAMP) (Li et al. 2020).

As incident polychromatic X-rays impinge on the quartz sample, crystal lattice planes in a certain orientation will interact constructively with the incident beam and produce a diffracted ray, given by Bragg's Law (Bragg and Bragg 1913). This diffraction can be written in terms of the Laue equations, from the perspective of polychromatic diffraction and the reciprocal lattice, but note that Bragg's Law can be derived from (has equivalencies with) the Laue equations that comprise the Laue condition for diffraction (Friedrich et al. 1912). Laue μXRD measures numerous microstructural properties, including the residual elastic strains in the crystal lattice (Noyan and Cohen 1987; Tamura et al. 2003; Robach et al. 2011). Laue diffraction spot positions can be used to measure the difference in unit cell shape between a deformed sample and undeformed standard. Each set of lattice planes that satisfies Bragg's Law (or equivalently the Laue condition) produces a spot on the diffraction pattern, whose position and shape are determined by the spacing and features of the lattice. Elastic deformation should produce variations in lattice and unit cell parameters that are able to relax after the imparted stress is removed. But if the deformation causes irreversible defects such as dislocations in the crystal, these defects "lock in" the elastic strains and prevent their relaxation. These residual strains manifest as

shifted diffraction spots relative to their unstrained (or reference) positions. Specifically, the change in shape of the unit cell at constant volume (deviatoric strain) produces a relative tilt of the lattice planes and results in a respective displacement of the Laue diffraction spots. The angular difference between these Laue diffraction spots are then used to quantify elastic deviatoric strain preserved in the crystal lattice (Fig. 2). The uncertainty in strain is impacted by the crystal lattice standard (quartz) and the number of indexed diffraction spots, automatically indexed by algorithms in XMAS (Tamura 2014). Previous studies using the same setup and instrumentation estimate an uncertainty of 0.3×10^{-3} strain using an unstrained hydrothermal quartz crystal as a standard, which translates to a stress uncertainty of 26 MPa, assuming a Young's Modulus 86.76 GPa. The most prominent factors that contribute to strain uncertainty are the accuracy of determining Laue reflection positions, CCD detector spatial correction, and calibration of experimental geometry (Poshadel et al. 2012).

Derivation of the deviatoric elastic strain tensor from the Laue diffraction pattern comes from the homogeneity property, which relates a deformed versus undeformed unit cell via a deformation matrix (Catti 1985; Chung and Ice 1999). The total elastic strain tensor ϵ_{ij} is then computed with the knowledge of the dilatational component of the strain, estimated by measuring the energy (or wavelength) of a single reflection in addition to the deviatoric strain tensor (Ice et al.

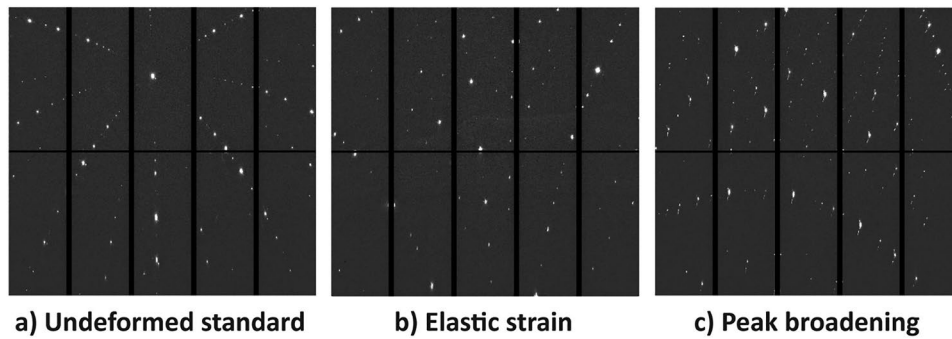


Fig. 2 Diffraction patterns of quartz collected using synchrotron Laue microdiffraction at the Advanced Light Source beamline 12.3.2 on a DECTRIS Pilatus 1 M detector. Each bright spot represents a set of coherently diffracting lattice planes in the unit cell, with the brightness directly proportional to the amount of coherent diffraction from each set of planes. **a** An unstrained hydrothermal quartz crystal standard. **b** A typical diffraction pattern for a crystal lattice with significant elastic strain. The angular difference between the position of these

spots and the corresponding spots in the undeformed crystal is used to calculate the residual strain. **c** A diffraction pattern with significant “smearing” of diffraction spots, which often arises from the presence of nonuniform plastic strain (dislocation density). Nonuniform strain produces a range of atomic spacings in the lattice that allow a broader range of Bragg angles to satisfy Bragg’s Law, resulting in broadening of diffraction peaks in diffractograms and smearing of diffraction spots

2000). The total strain tensor (with components ϵ_{11} , ϵ_{12} , ϵ_{13} , ϵ_{22} , ϵ_{23} , ϵ_{33}) at each scan spot is used to obtain the total stress tensor σ_{ij} with Hooke’s Law, and the elastic stiffness tensor of α -quartz at room temperature

$$C_{ijkl} = \begin{bmatrix} 0.8676 & 0.0687 & 0.1185 & -0.1802 & 0.0000 & 0.0000 \\ 0.0687 & 0.8676 & 0.1185 & 0.1802 & 0.0000 & 0.0000 \\ 0.1185 & 0.1185 & 1.0550 & 0.0000 & 0.0000 & 0.0000 \\ -0.1802 & 0.1802 & 0.0000 & 0.5814 & 0.0000 & 0.0000 \\ 0.0000 & 0.0000 & 0.0000 & 0.0000 & 0.5814 & -0.1802 \\ 0.0000 & 0.0000 & 0.0000 & 0.0000 & -0.1802 & 0.3995 \end{bmatrix}$$

in 10^{-2} GPa (Tamura 2014). Elastic anisotropy is accounted for in the calculated stress tensor using knowledge of the crystal orientation during strain refinement processes in the XMAS software. Stress maps presented in this study show equivalent stress σ_{eq} , a scalar quantity representing the magnitude of multiaxial elastic deviatoric stress at each scan spot (pixel),

$$\sigma_{eq} = \sqrt{\frac{(\sigma_{11} - \sigma_{22})^2 + (\sigma_{11} - \sigma_{33})^2 + (\sigma_{22} - \sigma_{33})^2 + 6(\sigma_{12}^2 + \sigma_{13}^2 + \sigma_{23}^2)}{2}}.$$

A detailed explanation of how strain and stress are measured and calculated using Laue microdiffraction is provided by Kunz et al. (2009), Tamura (2014), Chen et al. (2015), and Wenk et al. (2020).

Laue diffraction patterns also record plastic deformation. Plastic deformation usually occurs through dislocation growth and migration (Chen et al. 2015). A sample with a significant amount of dislocations will produce a distribution of local lattice plane tilts that upon summation directly

broadens the diffraction peaks (Tamura 2014; Zhou et al. 2016). Here, diffraction peak width is the average of the full width at half maximum of the diffraction peaks that comprise each diffraction pattern (pixel) taken in the Region of Interest (ROI). Observed peak width variations in single crystals arise from contributions predominantly from plastic strain, but can also be influenced by the instrumental profile and more subtly temperature and compositional effects (Warren and Averbach 1950; Warren 1959; Zhao and Zhang 2008). Because experimental conditions and instrumental contributions are constant throughout data collection, we assume that the majority of the observed variation in all peak width maps predominantly arises from sample variations in plastic strain (dislocation and defect density) (Fig. 3). The presence of geometrically necessary dislocations (GND) will cause asymmetric broadening and streaking of the Laue peaks (Barabash et al. 2002; Barabash and Ice 2005; Magid

et al. 2009; Budiman et al. 2015). Calculating misorientation between two adjacent points in the sample ROI can also be used as a proxy for density of GND (Wheeler et al. 2001; Hughes et al. 2003; Magid et al. 2004, 2009). Misorientation is a measure of the degree of crystal lattice orientation at a single scan spot in the crystal relative to the lattice orientation of adjacent (upper and right) scan spots (Fig. 4). Misorientation between two adjacent scan spots is quantified by two crystal orientation matrices, G_1 and G_2 , each the product of a rotational matrix R and transformation matrix L that

Fig. 3 Maps of average diffracton peak width (°) in the quartz crystal lattice surrounding melt inclusions from six rhyolitic volcanic systems. Melt inclusion photomicrographs are superimposed on each map for reference. Anomalous white patches are areas where there were not enough indexable diffraction spots to confidently quantify peak width. Scale bars are 100 µm

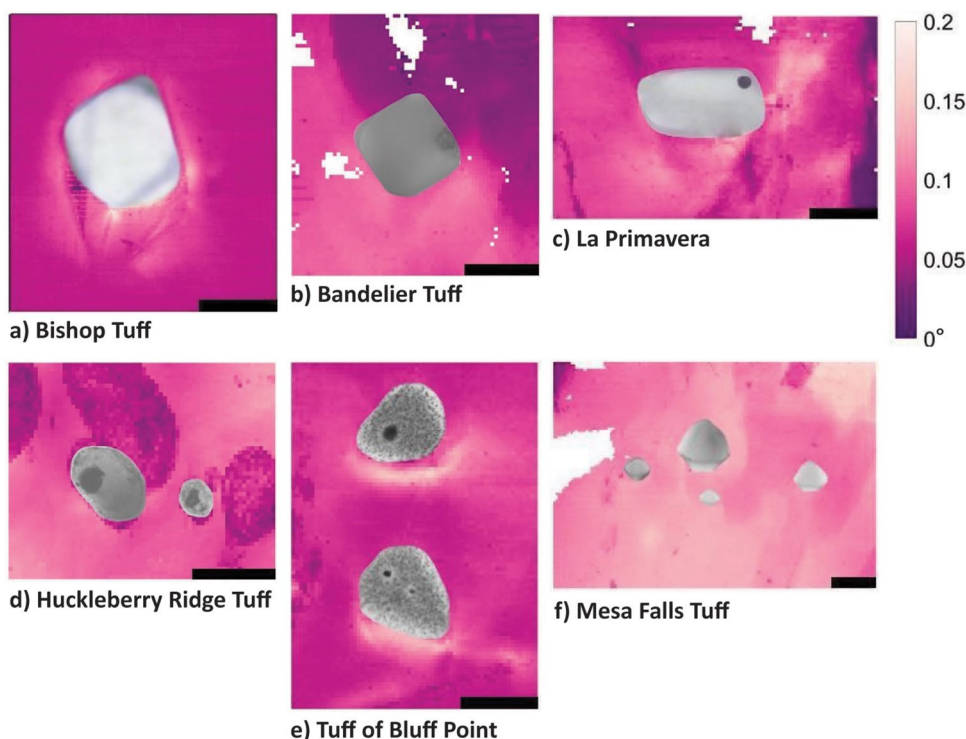
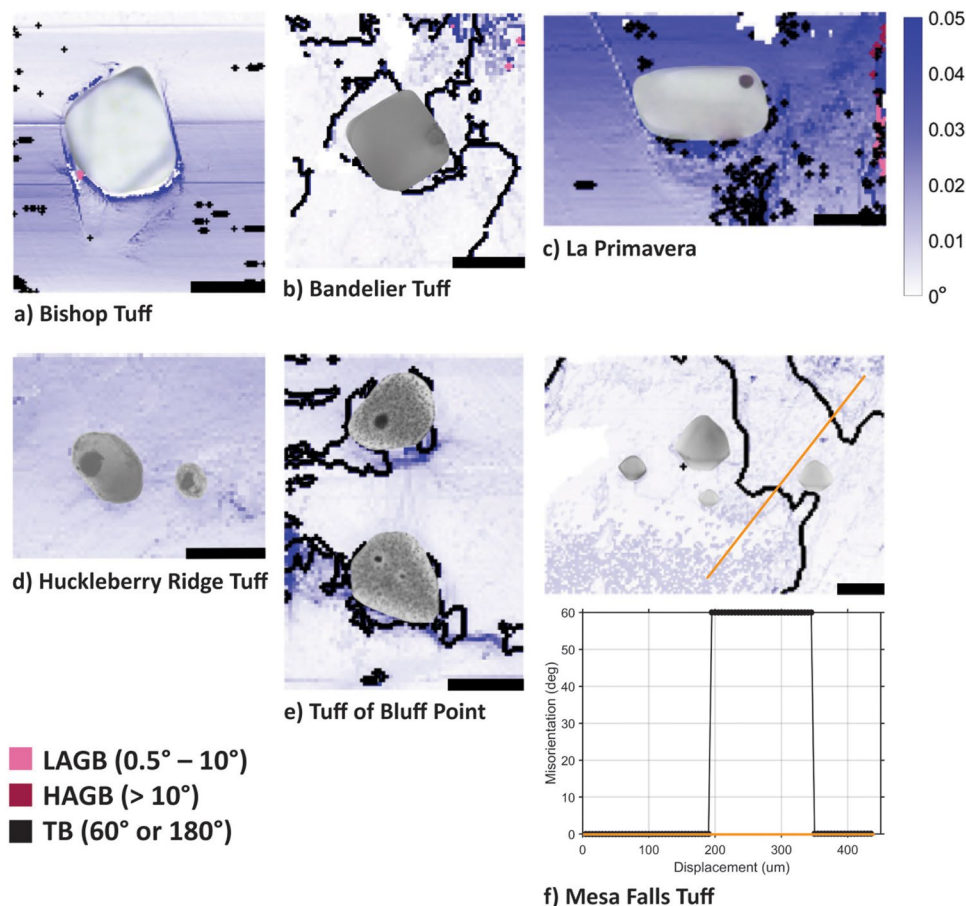


Fig. 4 Misorientation (°) maps where each pixel is colored by the degree of lattice orientation difference between adjacent pixels. The blue scale bars show low magnitudes of misorientation (<0.1°). Light pink lines show low-angle grain boundaries (LAGB), consisting of small misorientations between 0.5° and 10°. Dark pink lines are high-angle subgrain boundaries (HAGB) where misorientation between scan spots is ≥ 10°. Black lines are twin boundaries (TB) that correspond to misorientations of 60° or 180° around the quartz c-axis [001], thus regarded as Dauphiné twins (here, all are 60°). The Mesa Falls map includes a linear misorientation distribution through the Dauphiné twin boundaries along the orange line, showing the change in misorientation between successive pixels along the line. Scale bars are 100 µm



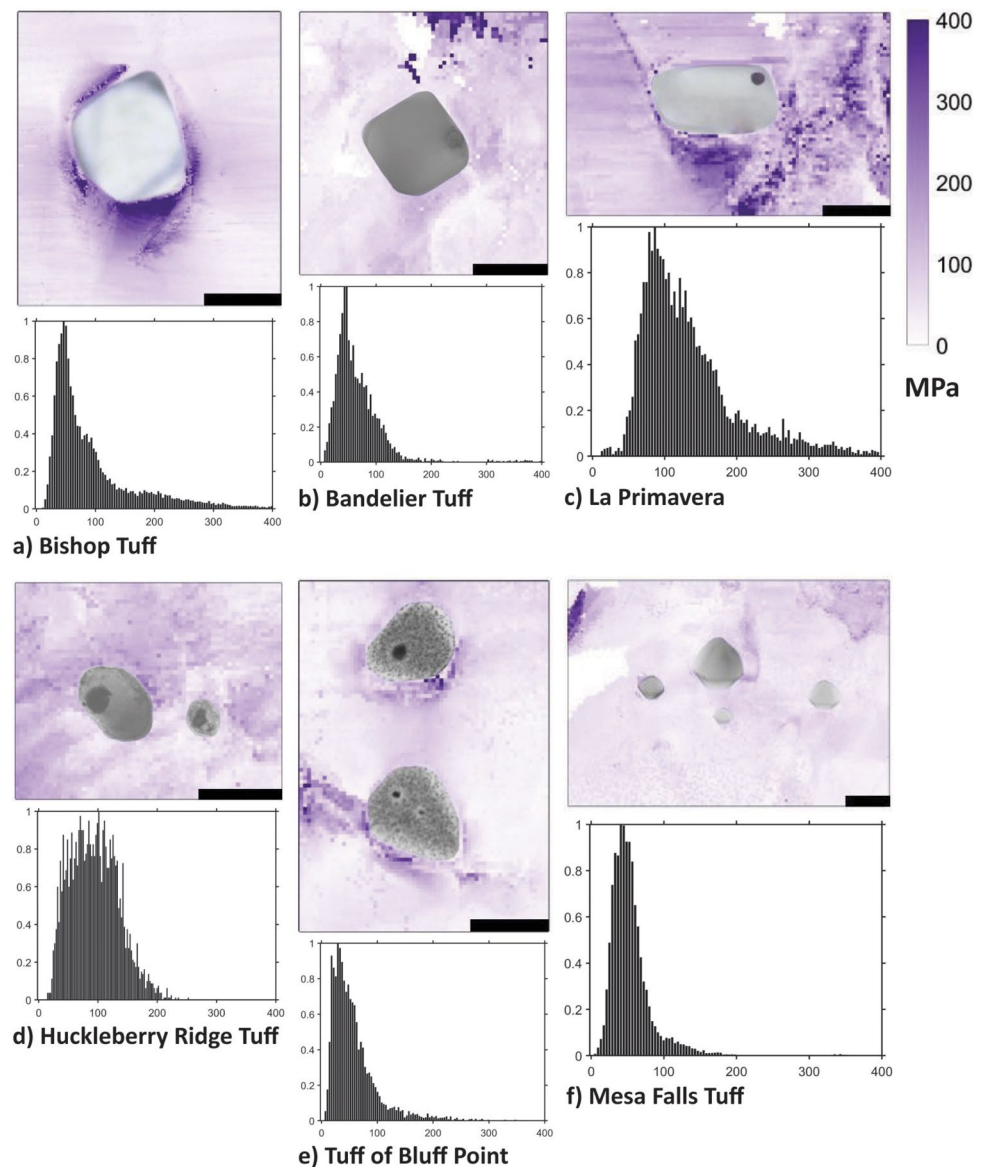
convert vectors and Miller indices from Cartesian to sample coordinates, respectively, such that

$$G = RL \quad \text{and} \quad M = G_1 G_2^{-1} = R_1 L L^{-1} R_2^{-1} = R_1 R_2^{-1}.$$

The misorientation matrix M is then a corresponding rotational matrix represented as an angle-axis pair between current spot P and its right (P_r) and upper (P_u) neighbors, given by $\{\theta_r, v_r\}$ and $\{\theta_u, v_u\}$, respectively. Boundaries are then categorized into low-angle (LAGB), high-angle (HAGB), and twin boundaries (TB) based on user-defined thresholds (provided in Fig. 4 legend) and criteria outlined in Li et al. (2015). The misorientation maps show the maximum value of misorientation between these values and denote LAGB, HAGB, and TB (Fig. 4). For single crystals,

the misorientation angle is directly proportional to (as it is caused by) the GND density (Wheeler et al. 2001; Hughes et al. 2003; Magid et al. 2004, 2009; Brewer et al. 2006). Because there can be multiple Bragg angles and X-ray energies for a given diffraction spot in a Laue pattern (per each map pixel), we deem an informal qualitative approach most prudent and are interested in the relative variation in peak width as it relates to variations in magnitude of preserved plastic strain (Moffat 2019). White patches in residual stress maps are areas of pixels that could not be indexed. There are small populations of stresses above 400 MPa (Fig. 5), but for inter-comparison and ease of seeing stress distributions on the map, the color bar has been set from 0 to 400 MPa for all samples.

Fig. 5 (Top) Maps of residual equivalent elastic stress in the quartz crystal lattice surrounding melt inclusions from six rhyolitic volcanic systems. Melt inclusion photomicrographs are superimposed on each map for reference. The color scale for MPa is the same for all maps and truncates at 400 MPa because the vast majority of stresses are below this value. Including higher values reduces the clarity of the fine scale distribution of stresses. Anomalous white patches are areas where there were not enough indexable diffraction spots to confidently quantify residual stress. Scale bars are 100 μm . (Bottom) Relative frequency of residual equivalent stress in each map in MPa



Results

Melt inclusion features

Our sample suite preserves a range of inclusion faceting, glasiness, and presence of bubbles and cracks (Fig. 1). Inclusions from Bishop Tuff and La Primavera are the most pristine, with clear glass free of visible signs of devitrification. The La Primavera inclusion contains a small bubble on the lower inclusion edge. The Bishop and La Primavera inclusions are partially faceted with rounded corners and beveled edges, with a faceting strength of 1.0 according to the Boro et al. (2021) scale. Mesa Falls and Bandelier Tuff inclusions are the most faceted with relatively straight edges and developed corners, with faceting strengths of 2.0 and 1.5, respectively. The distinction between the faceting strengths is because the Mesa Falls inclusions have sharp corners whereas the Bandelier inclusion corners are still rounded. Bandelier also has a small bubble. Both Mesa and Bandelier inclusions are slightly fuzzy and brown which indicates the presence of incipient crystallites (devitrification). The Huckleberry Ridge Tuff and Tuff of Bluff Point inclusions appear most affected by devitrification, and all contain bubbles (with the bottom Bluff Point inclusion containing two bubbles). The Tuff of Bluff Point inclusions have a faceting strength of 1.5, with straight edges and rounded corners, The Bluff Point inclusions are also heavily devitrified, with relatively coarse crystallites distributed throughout the inclusion interior. The Huckleberry Ridge inclusions also have appreciable devitrification given their dark brown appearance. The Huckleberry inclusions are the least faceted compared to the other samples (faceting strength of 0.5), with rounded sides and undeveloped corners. The observed 2D shape of the inclusions can be influenced by the angle that the sample is polished in relation to the inclusion geometry, but these effects overall are relatively minor and would not affect their placement on the faceting scale by more than one grading. An equivalent spherical radius for each

inclusion was measured in *Fiji* (Schindelin et al. 2012) and faceting times calculated from these radii are all on the order of 10^2 – 10^3 years, using trapping temperatures in Table 2 (Gualda et al. 2012).

Residual strain

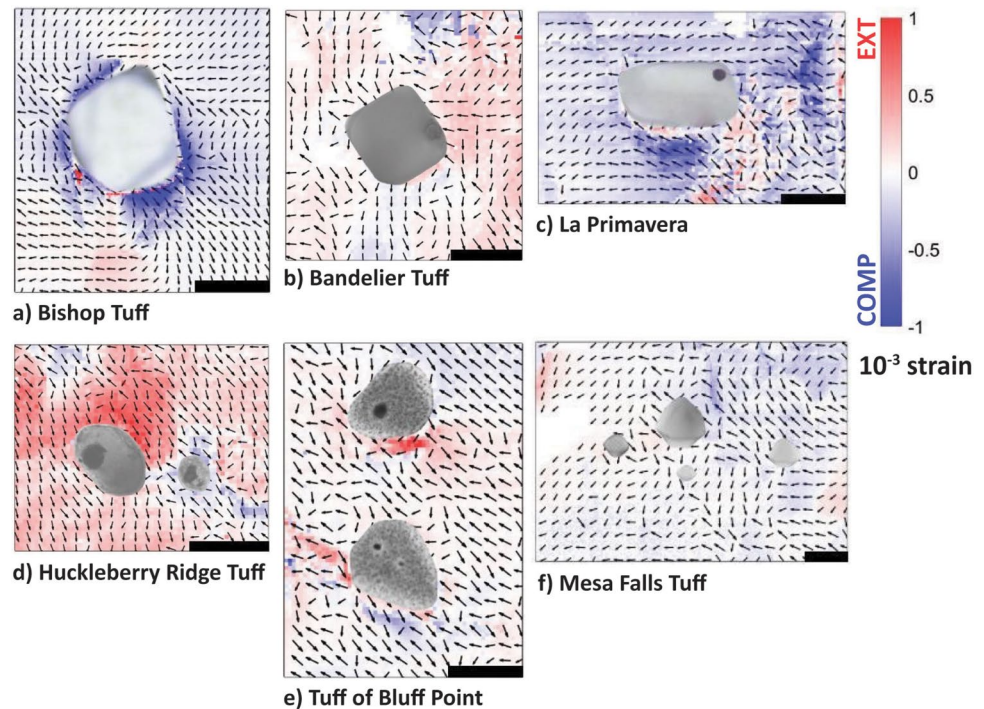
Maps of residual elastic strain show consistent results in all samples (Fig. 6). Strain values range from approximately -1.5×10^{-3} to 1.5×10^{-3} strain across all samples. Specific ranges for each sample are as follows (all in units of 10^{-3} strain): Bishop – 1.86 to 2.14, Bandelier – 0.75 to 1.53, La Primavera – 1.55 to 1.71, Huckleberry Ridge – 0.60 to 1.02, Bluff Point – 1.06 to 1.29, and Mesa Falls – 0.60 to 0.53. There is a clear impact on lattice strain from the inclusions' presence most prominently in the Bishop map, but also in the La Primavera and Bluff Point maps. The impact of the inclusions' presence is not obvious in the Bandelier, Huckleberry Ridge, and Mesa Falls maps. Compressive strain is elevated around the Bishop inclusion, most concentrated in the lower boundary, and decays away from the inclusion border. The Bandelier sample has strain magnitudes comparable to La Primavera, but shows only a mottled distribution of strain in the ROI. The La Primavera sample shows impact from both the inclusion and crack, with elevated strain on the lower and right inclusion margins. The elevated strain is also of differing sense (both extensional and compressional) throughout this region. The Huckleberry Ridge inclusion shows a broad distribution of elevated extensional strain across the ROI, contributed to by the many inclusions around and deeper in the sample. The Bluff Point sample has relatively high magnitudes of preserved strain, the highest values ($\sim 1.2 \times 10^{-3}$ strain) existing along the lower border of the upper inclusion. There are notable amounts of both compressional and extensional strain preserved around the crack (Fig. 6e). Interestingly, the Bluff Point inclusions both show elevated strain around their lower margins but with opposing sense—the top preserving extension, the bottom compression. The Mesa Falls ROI preserves the lowest magnitude strain and displays mostly compressional strain that

Table 2 Melt inclusion (MI) trapping temperature, calculated glass transition temperature from Table 4 values and Giordano et al. (2008), and MI storage (volatile saturation) pressures

MI sample	Trapping T (°C)	Glass transition (°C)	Storage pressure (MPa)	References
BT	725	413	100–230	Anderson et al. (2000)
BaT	700	390	100–143	Waelkens et al. (2022)
LP	750	372	200	Sosa-Ceballos (2015)
HRT	800 ± 24	438	~ 100	Myers et al. (2016)
TBP	750 ± 25	472	90–150	Befus and Gardner (2016)
MFT	800–835	439	100–150	Tollan et al. (2019)

BT = Bishop Tuff, BaT = Bandelier Tuff, LP = La Primavera, HRT = Huckleberry Ridge Tuff, TBP = Tuff of Bluff Point, MFT = Mesa Falls Tuff

Fig. 6 Maps of residual strain in the quartz crystal lattice. Melt inclusion photomicrographs are superimposed on each map for reference. Color scale is in 10^{-3} strain, where red is extensional and blue is compressive strain. Vectors show the in-plane projection of the direction of the principal component of the strain tensor in the lattice (i.e., the orientation of the extensional strain axis), where the arrow length corresponds to the amount of axis tilt in or out of the 2D projection. Anomalous white patches are areas where there were not enough indexable diffraction spots to confidently quantify residual strain. Scale bars are 100 μm



does not necessarily correlate with the inclusions' locations. Notably, the samples with cracks in their ROI (La Primavera and Bluff Point) do not record the highest strain of all samples, whereas samples with larger or similar strains (Bishop, Bandelier) do not have cracks. Moreover, inclusions are all of similar size ($\sim 100\text{--}200\ \mu\text{m}$) but Bishop and La Primavera are the largest, the Primavera inclusion also having the largest aspect ratio (~ 2). Importantly, most crystals record a disturbance in the magnitude and orientation of their strain fields around the inclusion displayed by the variable in-plane stretching direction of the lattice (e.g., the arrows in Fig. 6). The directionality of the strain field does not appear in some residual stress or strain maps themselves, but strain fields are clearly impacted proximal to the inclusions in all samples.

Residual stress

Residual stress maps show similar magnitudes of stress in all samples, with means and medians ranging from 53–135 MPa to 46–116 MPa, respectively (Fig. 5, Table 3). All samples possess positive skewness in their residual stress distributions, with Bishop and La Primavera having the longest tails (Fig. 5a, c). Average residual stress values for each sample are: Bishop Tuff (84 MPa), Bandelier Tuff (66 MPa), La Primavera (135 MPa), Huckleberry Ridge Tuff (94 MPa), Tuff of Bluff Point (59 MPa), Mesa Falls Tuff (54 MPa). These values align with previous residual stress studies of volcanic crystals (Befus et al. 2019). Though similar in magnitude, the spatial distribution of residual stresses varies considerably between each sample. Inclusion faceting strength does

not appear to correlate with preserved residual stress or strain, nor the calculated stress associated with the thermal volume change of the inclusions (Fig. 7). The presence of bubbles in the inclusion glass does not seem to contribute to the crystal stress distributions.

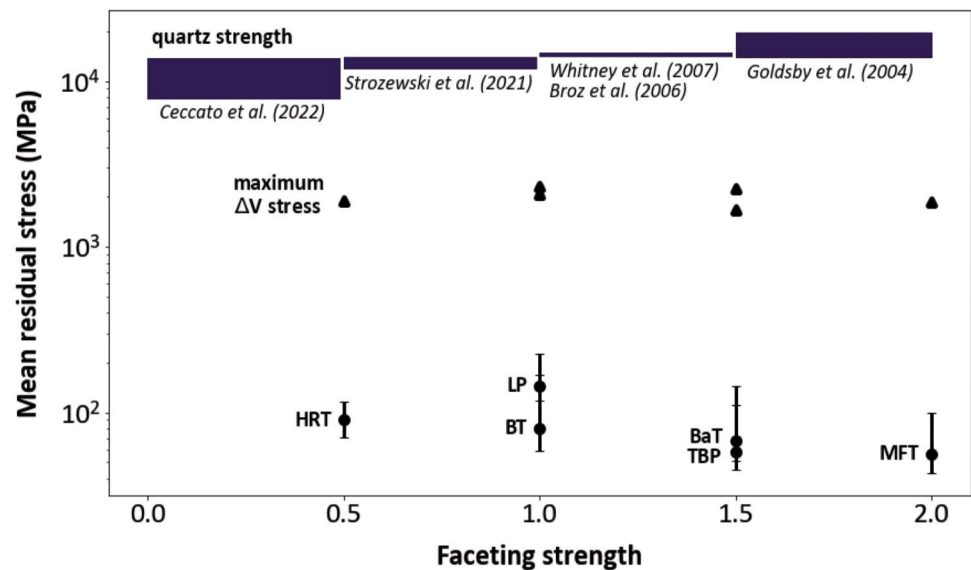
Residual stresses are most commonly the highest near inclusions. Such distributions are pronounced in the Bishop Tuff, La Primavera, and Tuff of Bluff Point crystals. The Bishop Tuff sample shows a relatively homogeneous and low ($< 100\ \text{MPa}$) distribution of stress $> 50\ \mu\text{m}$ from the inclusion, but there is a concentration of elevated residual stress ($\sim 300\text{--}400\ \text{MPa}$) within $50\text{--}100\ \mu\text{m}$ of at least one inclusion boundary (Fig. 5). Elevated stress near inclusions is also demonstrated texturally as pre-existing cracks radiate from inclusions in the Tuff of Bluff Point and La Primavera quartz. Quartz from the Tuff of Bluff Point preserves a region of elevated residual stress along the lower margins of both inclusions ($\sim 120\text{--}300\ \text{MPa}$), both extending up to about $50\ \mu\text{m}$. The elevated residual stress also extends at least $100\ \mu\text{m}$ further along the trend of the preexisting crack, but its total length extends past the mapped field of view (Fig. 5e). Residual stresses also increase along some of the margins of the La Primavera inclusion, again extending $\sim 150\text{--}200\ \mu\text{m}$ from the inclusion boundary (right side in Fig. 5c). The extent of the residual stresses correlates with the length of a crack in the La Primavera crystal. In other locations surrounding the inclusion the stress distributions are striped and muddled and spread away from the crack propagating through inclusion to the lower right. In the rightmost La Primavera ROI, there are vertically oriented

Table 3 Mean residual stress from Fig. 3 (with asymmetric deviations above and below the mean) and calculated magma residence times for each system

Eruptive unit	Mean residual stress $\pm 1\sigma$ (MPa)	Median residual stress $\pm 1\sigma$ (MPa)	Magma residence time	References
Bishop Tuff	84 ⁺⁸⁸ ₋₂₂	61 ⁺⁸⁴ ₋₁₇	100 k.y.–1 M.y 300 k.y < 100 k.y 50–80 k.y < 10 k.y.* < 10 k.y	Anderson et al. (2000) Christiansen and Halliday (1996) Reid and Coath (2000) Crowley et al. (2007) Gualda et al. (2012) Hervig and Dunbar (1992)
Bandelier Tuff	66 ⁺⁷⁷ ₋₁₇	53 ⁺⁷¹ ₋₁₄	1–200 y.*	Winick et al. (2001)
La Primavera	135 ⁺⁸¹ ₋₂₇	116 ⁺⁷⁹ ₋₂₃	–	–
Huckleberry Ridge Tuff	94 ⁺²⁶ ₋₁₉	92 ⁺²⁶ ₋₁₉	77–234 k.y	Christiansen (2001)
Tuff of Bluff Point	59 ⁺⁵² ₋₁₃	46 ⁺⁴⁹ ₋₁₀	≥ 90 k.y.*	Watts et al. (2012)
Mesa Falls Tuff	54 ⁺⁴³ ₋₁₃	47 ⁺⁴⁰ ₋₁₂	160–170 k.y	Christiansen (2001)

Magma residence times are calculated by taking the difference between the eruption ages (Ar/Ar) and radioactive clocks (U–Th–Pb in zircons), compiled by Costa (2008). Times marked with an asterisk are other forms of approximation where other data was not available (Bishop Tuff: MI faceting, crystal size distributions, rhyolite-MELTS simulations; Bandelier Tuff: oxygen isotopes diffusion modeling, Tuff of Bluff Point: comparing early to late Yellowstone Central Plateau Member eruption ages)

Fig. 7 Average residual stress (MPa) in quartz around inclusions vs. faceting strength of melt inclusions using the Boro et al. (2021) scale (black dots). Higher faceting strength means straighter edges and sharper corners. Black triangles are maximum calculated stress associated with thermal inclusion-host volume change for each sample (Fig. 10). Vertical bars on residual stresses are asymmetric standard deviations above and below the mean (Table 3). Quartz strengths plotted for reference



structures in the peak width, strain, and stress maps that are near a short, thin crack on the right side of the inclusion, but are spatially shifted from this feature (Figs. 1c, 3c, 5c, and 6c). There are elevated residual stresses on the right La Primavera inclusion border that correlate with this small crack (Fig. 5c). The large patch of higher residual stress (~300–500 MPa) toward the bottom of the La Primavera ROI (Fig. 5c) may also be contributed to by deeper inclusions (Fig. 1). The distribution of residual stresses surrounding inclusions from the Bandelier Tuff and Mesa Falls Tuff

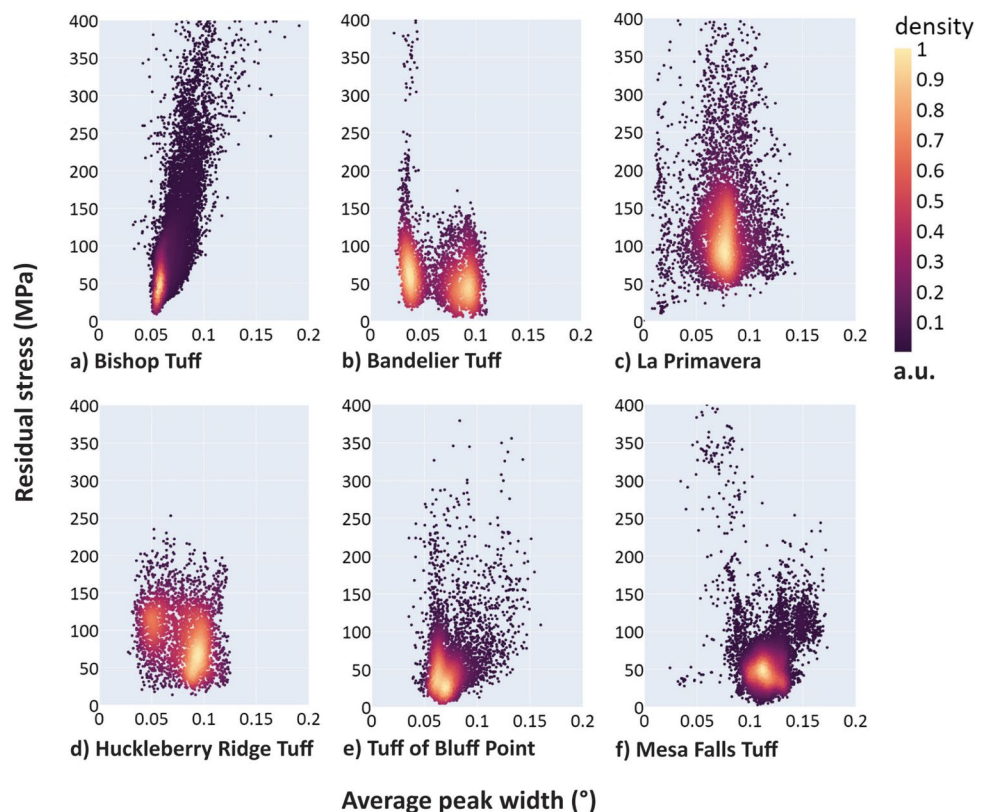
do not show an obvious relationship to the presence of the inclusions. The distribution in the Huckleberry Ridge Tuff is less clear. The Huckleberry Ridge Tuff map has the second highest mean residual stress of all samples and the broadest spread of stress values (Fig. 5d). Deeper inclusions may moderately elevate the stress measured at the surface of the sample (e.g., darker areas to the upper right of both surface inclusions in Fig. 5d).

Diffraction peak width

All samples preserve plastic strain as recorded by peak widths (Fig. 3). In most samples the quartz host shows a rather uniform distribution of peak widths ranging from 0.01° to 0.19° . The Bishop Tuff peak width map echoes its residual strain and stress maps, with elevated peak widths that tightly wrap the inclusion borders and taper off to background values of approximately 0.05 – 0.08° . The Bandelier map does not show high peak widths around the inclusion, but instead shows a division of high and low peak widths across the map, uniform in each region and divided with a curved border that cuts across the inclusion and aligns diagonally with two inclusion apices. The La Primavera ROI shows low peak widths near the cross-cutting crack, yet higher values along the lower and right inclusion borders, similar to the residual strain and stress maps. With relatively high peak widths that fan out away from the right and bottom sides of the inclusion, there is also a quasilinear patch of very low ($\leq 0.03^\circ$) peak widths spanning the rightmost portion of the ROI. The Huckleberry Ridge map shows elevated peak widths of 0.10 – 0.14° across the entire ROI except for the locations of the inclusions, even those deeper in the crystal. The peak widths in the Bluff Point sample are elevated (at least $+0.1^\circ$ compared to other areas in the ROI) in the same areas of higher signal in the strain and stress maps, except the higher peak widths do not extend across the

crack on the left of the lower inclusion (and are limited to the lower inclusion margin) unlike the other maps. The elevated peak widths on the upper inclusion display an arcuate trend that follows the lower border of the inclusion, whereas the bottom inclusion peak widths are straight and extend only to the lower right where the crack also continues. In this way, the La Primavera and lower Bluff Point inclusion demonstrate opposite trends for peak width magnitudes relative to background along each crack: The La Primavera inclusion shows lower preserved plastic strains than background over the length of the crack whereas that of the Bluff Point inclusion are higher than background. Similar to the Huckleberry map, the Mesa Falls peak width map shows elevated peak widths of ~ 0.12 – 0.17° distributed rather uniformly across the map, with an unstructured patch of lower values on the right side (which includes one of four inclusions). Areas of elevated proximal stresses for two inclusions (Bishop Tuff and Tuff of Bluff Point) appear to minorly spatially correlate with elevated peak widths, but throughout both ROIs, and more broadly all studied samples, there is no significant relationship between residual stress and peak width (Fig. 8). Depth averaging of the X-ray signal is most evident in the Huckleberry Ridge map where inclusions ~ 50 – $200 \mu\text{m}$ below the surface modify the peak width signal (Figs. 1d and 3d).

Fig. 8 Scatter plots of residual stress vs. average peak width, where each point corresponds to each pixel on the corresponding map. Because there are thousands of points that result in significant overlap on each plot, points are colored by a Gaussian kernel density estimation, where higher density of points corresponds to color bar values closer to unity. All crystals (except Bishop minorly) do not demonstrate a significant relationship between residual stress and average peak width, with R^2 values of Bishop Tuff = 0.622, Bandelier Tuff = 0.016, La Primavera = 0.0002, Huckleberry Ridge Tuff = 0.008, Tuff of Bluff Point = 0.007, Mesa Falls Tuff = 0.094



Misorientation and twin boundaries

Calculating misorientation provides another assessment of plastic strain given its direct relationship to dislocation (GND) density. Quartz samples in this study all demonstrate relatively low background misorientations of near zero to 0.1° (Fig. 4). The magnitude of misorientation is similar between maps, and misorientation distributions echo distributions of stress and strain in their corresponding peak width, strain, and stress maps (Figs. 3, 5, and 6). But unlike the microstructural maps discussed thus far, most misorientation maps show patterns that can be clearly related to the inclusions. The quartz lattice bordering the inclusions (most notably Bishop, La Primavera, and Bluff Point) shows markedly high misorientations from background that wrap or radiate away from the inclusion locations. The Huckleberry Ridge and Mesa Falls maps show subtle elevated misorientations around the inclusion boundary, mostly on the lower borders. The Bishop ROI shows a large horizontal stripe of misorientation around 0.015° , compared to the darker blue region above around 0.004° and thin patch in the lower ROI of 0.01° (Fig. 4a). The magnitudes of elevated misorientations bordering the inclusion are generally 0.04° – 0.14° , but as high as 0.3° . The Bandelier ROI shows higher background misorientation in the top right (0.03° – 0.46°), similar to distributions observed in the strain and stress maps (Figs. 5 and 6). There are three small regions where misorientation is at or slightly above 0.5° , qualifying these zones as low-angle grain boundaries (LAGB) (Menegon et al. 2011; Li et al. 2015). The Bandelier map is the only map that does not show any impact of the inclusion on background misorientation (Fig. 4b). The background misorientation values are highest overall in the La Primavera sample, increasing from 0.01° to 0.03° towards the upper ROI (Fig. 4c). The highest values on the lower inclusion border and right side of the ROI range from 0.2° to 4° . The crack in the La Primavera ROI is highlighted by the elevated misorientation along its length, both above and below the inclusion, similar to its peak width, strain, and stress maps (Figs. 3c, 5c, and 6c). The signatures on the right side of the La Primavera peak width, strain, and stress maps are also reflected in the misorientation map (Figs. 3c, 4c, 5c, and 6c). This area (rightmost ROI) demonstrates both low-angle and high-angle grain boundaries, with misorientations between 0.5° and 10° and $\geq 10^\circ$, respectively (and Dauphiné twins, discussed below) (Fig. 4c). Interestingly, the Huckleberry Ridge ROI only displays very low misorientations between 0.001° and 0.027° , but no evidence of intragrain boundaries (Fig. 4d). The Tuff of Bluff Point ROI has background values of 0.001° – 0.06° , with elevated values of 0.08° – 0.11° near the leftmost ROI around the crack, but also propagates below it (comparing Figs. 1e, 2e, 3e, 4e). Mesa Falls background misorientation values are approximately 0° – 0.045° ,

near the top right of the map. There are slightly elevated misorientations ($+0.015^\circ$) around Mesa Falls inclusion borders (Fig. 4f). Neither Bluff Point nor Mesa Falls display low-angle or high-angle grain boundaries.

All samples except Huckleberry Ridge have twin boundaries (Fig. 4). Bishop and La Primavera show dots or clusters of twin boundaries (Fig. 4a, c) and Bandelier, Bluff Point, and Mesa Falls display meandering, continuous twin boundaries (Fig. 4b, e, f). Twin boundaries in all maps are characterized by misorientation values of 60° about the α -quartz c-axis ([0001]), establishing these features as Dauphiné twins (Fron del 1962; Li et al. 2015). The Bishop twin boundaries are scattered throughout the ROI and are not spatially coincident with other observed microstructures, strain, or stresses. The Bandelier twin boundaries do not show a clear correlation with the distribution of peak widths, strains, or stresses, except for a short twin boundary towards the top middle that overlaps with the only area of elevated stresses in the ROI (Figs. 4b and 5b). The La Primavera twin boundaries do show clustering in the lower ROI that overlaps with elevated strain and stress (Figs. 4c, 5c, and 6c). The Bluff Point twin boundaries show clear overlap with the elevated strains and stresses present in the ROI (particularly along the crack on both sides of the lower inclusion), with more twin boundaries in the upper left ROI where there is no obvious elevated peak width, strain, or stress (Figs. 4e, 5e, and 6e). The Mesa Falls ROI shows clear Dauphiné twin boundaries that closely align with its peak width distribution (Figs. 3f and 4f), and to a lesser extent the strain and stress distributions (Figs. 5f and 6f). The Mesa Falls misorientation panel includes a linear misorientation distribution indicated by the orange line to show the 60° misorientations that establish the Dauphiné twin (Fig. 4f).

Discussion

In general, strain and stress across eruptions are of similar magnitude (on the orders of 10^{-3} strain and $\sim 10^2$ MPa). This suggests that these magnitudes are caused by forces that are ubiquitous between these studied eruptions, such as similar amounts of thermal contraction, conduit shearing, and ascent rates, constrained by the ability of the quartz host to record these processes. Studied deposits have similar storage temperatures (~ 700 – 800°C) (Table 2). Available magma ascent rates calculated from volatile diffusion modeling are also similar: Bishop Tuff 0.6 – 13 m s^{-1} with 75% of results in the range 0.4 – 5 m s^{-1} (Myers et al. 2018), Bandelier Tuff 0.01 – 4 m s^{-1} (Saalfeld et al. 2022), Huckleberry Ridge Tuff 0.3 – 4.0 m s^{-1} (Myers et al. 2018), and Mesa Falls Tuff 0.005 – 0.08 m s^{-1} (Befus et al. 2023).

It is not immediately apparent if all studied crystals experience or record strains and stresses from the multitude

of processes that could deform them. There is no clear correlation between elastic and plastic strain in all samples, except Bishop minorly with $R^2 \approx 0.6$ (Fig. 8). Compared to background levels, elevated strains, stresses, peak widths, and misorientations are observed around inclusions and cracks. Notably, stress-free haloes do not exist around faceted inclusions. To better understand what processes may contribute to residual strain and stress in these crystals, we discuss potential strain and stress contributions chronologically, from the time of crystal growth in the magma system to deposition on Earth's surface.

Crystal growth

Residence times estimated from the difference between zircon ages and eruption ages share similar magnitudes of $\sim 10^5$ years (Table 3 and references therein), approximating the timescale that quartz existed in the magma chamber before eruption. These timescales are consistent with those estimated for the formation of large relatively crystal-poor rhyolite mushes in the upper crust of 10^4 – 10^5 years (Bachmann and Bergantz 2004; Seropian et al. 2018; van Zalinge et al. 2022). Petrologic studies give a range of quartz residence times for rhyolitic magmas in the crust using elemental diffusion chronometry, from a few years to tens to hundreds of thousands of years (Gualda et al. 2012; Seitz et al. 2016; Audétat et al. 2023). Van den Bogaard and Schirnick (1995) found that quartz phenocrysts from the Bishop Tuff crystallized, trapped glass inclusions, and became a closed system with respect to Ar at 1.89 ± 0.03 to 2.3 ± 0.3 Ma, which are much older than the eruption age ~ 765 ka. Given these ages, the magma crystal cargo may experience a protracted and varied strain history during its lifetime in the reservoir, accruing strains from cycles of magma injection, mush compaction, and crystal force chains, followed by further stresses during fragmentation and ascent.

Stressful events begin introducing and establishing dislocations and defects that lock in elastic strains and provide avenues for plastic deformation, which will later influence how the crystal accommodates and preserves strain in the shallow chamber and subsequent eruption. On these protracted $\sim 10^5$ – 10^6 year timescales, it is possible that the residual strain and stress acquired in a quartz crystal may be “erased” or “reset” upon mineral dissolution and regrowth. This may mean that the cores of crystals preserve higher stresses than the rims, but this was not systematically observed in Befus et al. (2019). There continues to be evidence for cold (near- or sub-solidus) magma storage, which may ultimately vary both from system to system and over time, as dictated by their tectonic setting, magmatic history, and structure of the surrounding crust (Barboni et al. 2016; Rubin et al. 2017; Cooper 2019). While cold storage

of crystal cargo may limit their potential for recrystallization or dissolution (also depending on the size and frequency of magma injection), crystals from all storage systems in this study preserve similar magnitudes of elastic stress, regardless of storage times, temperatures, eruption type, and volume (Table 1).

Mush compaction

Mushes are thought to compact via crystal repacking (mechanical compaction) or crystal deformation (viscous compaction) depending on the crystallinity (Holness et al. 2017; Bachmann and Huber 2019). In crystal-rich magma reservoirs, mush compaction can impart significant plastic deformation on crystals via dislocation creep (Holness et al. 2017; Holness 2018). This may be the primary mechanism by which weaker phases (such as quartz) begin acquiring statistically stored dislocations (SSD) and geometrically necessary dislocations (GND) that both record plastic strain and elastic strain by preventing its total relaxation. Erupted crystallinities for studied deposits here are $< 20\%$, but may not represent what was present in the reservoir to facilitate compaction and possible force chains (Bergantz et al. 2017). That is, it is possible and accepted that melt segregation during final magma assembly forms crystal-poor magmas from crystal-rich sources (Gualda et al. 2019).

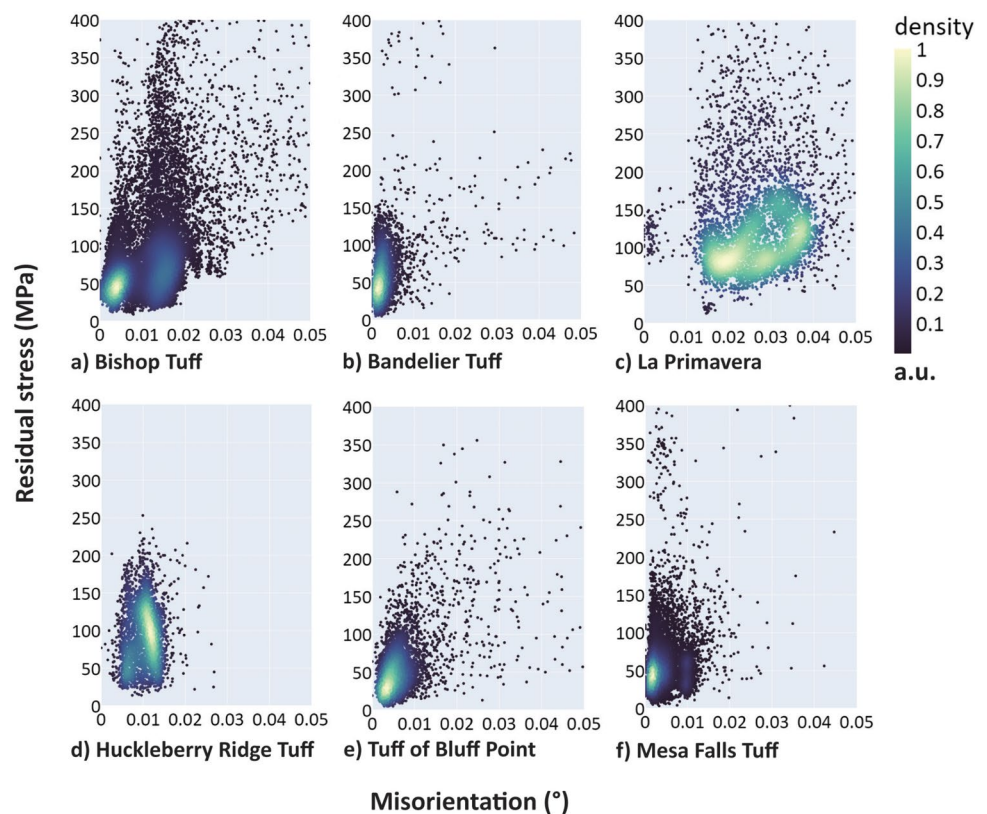
The heterogeneity of dislocation and twin distributions in deformed and deforming crystals gives rise to irregular lattice curvatures, causing variations in lattice orientation that can be quantified and visualized as lattice misorientation maps. The misorientation maps show varying degrees of plastic strain around the inclusions and highlight various subgrain boundaries in the ROIs (Fig. 4). Similar to the residual stress and strain maps, there are clear elevated misorientations compared to background in the Bishop, La Primavera, and Bluff Point maps. There are subtler elevated misorientations (in terms of both magnitude and distribution) in Huckleberry Ridge and Mesa Falls, and basically indistinguishable values of misorientation around the Bandelier inclusion compared to background values.

Background misorientations below 0.5° are a sign of low deformation or straining. In fact, most background strains in the studied ROIs are an order of magnitude lower than this threshold ($\sim 0.05^\circ$) and are highest in the La Primavera quartz (which also demonstrates pervasive low-angle, high-angle, and twin boundaries). All samples except Huckleberry Ridge have pervasive Dauphiné twins, with the La Primavera and Bluff Point twin boundaries mostly co-located with elevated misorientations and residual stresses (Figs. 4 and 5). Bandelier has pervasive Dauphiné twin boundaries, but minimal residual stress and strain (elastic and plastic) throughout the ROI.

Dauphiné twinning can be primary, forming during crystal growth, or secondary, or a result of mechanical or transformational effects (e.g., Straumanis 1949; Van Tendeloo et al. 1976; Heaney and Veblen 1991; Piazzolo et al. 2005; Wenk et al. 2009; Li et al. 2015). Transformational Dauphiné twinning occurs at the high-to-low quartz phase transition at 573 °C (at atmospheric pressure) from slight atomic displacements caused by thermal vibrations. Mechanical Dauphiné twinning is induced by stress, and its initiation and persistence are highly dependent on the crystallographic orientation of the quartz crystal with respect to principal stresses. In fact, both dislocations and Dauphiné twins can only nucleate and migrate on crystallographic planes with a high or critical resolved shear stress (Tullis and Tullis 1972; McLellan 1978). Dauphiné twinning is particularly sensitive to local stress variations and attempts to align the direction of greater elastic compliance in the crystal to the principal compression axis, again dependent on the crystal orientation with respect to the applied stress (Wenk et al. 2007, 2009). This requirement can explain why Dauphiné twinning is not distributed homogeneously across sample ROIs or is entirely absent from the chosen ROI (but may be present elsewhere in the crystal). As the maps are only two-dimensional slices of the crystal, it is possible that there are other twin and dislocation networks in other cuts through the three-dimensional crystal, or in other areas that were not imaged.

Although dislocation networks produce both elastic and plastic strain fields (Wilkinson et al. 2014), we do not observe correlations between residual stress (elastic strain) and misorientation or peak width (plastic strain) (Figs. 8 and 9). Co-location of elevated residual stress and misorientation (including twins and subgrain boundaries) around the Bishop Tuff, La Primavera, and Tuff of Bluff Point inclusions are not tightly associated from pixel to pixel (Fig. 9). This may be a result of other elastic deformation sources (e.g., shearing during fragmentation, Eshelby stresses from pressure changes), or could reflect a crystallographic control on the availability of dislocation slip systems to activate and grow given the crystal orientation with respect to applied stresses during mush compaction. We hypothesize that quartz crystals take on most of their residual plastic strain during viscous mush compaction over their long storage timescales prior to eruption. As the presence of Dauphiné twins exerts a considerable impact on the partitioning and localization of plastic strain, these twins (and dislocations) will set the stage for how later deformation will be experienced and then recorded in each crystal (Menegon et al. 2011). Furthermore, these pervasive dislocation and twin networks may become tangled and thus form pathways for crystals to fail (crack) or lock in imparted elastic strains during eruption.

Fig. 9 Scatter plots of residual stress vs. misorientation, where each point corresponds to each pixel on the corresponding map. Points are colored by a Gaussian kernel density estimation, where higher density of points corresponds to color bar values closer to unity. No crystals demonstrate a significant relationship between residual stress and misorientation, with R^2 values of Bishop Tuff=0.002, Bandelier Tuff=0.006, La Primavera=0.019, Huckleberry Ridge Tuff=0.004, Tuff of Bluff Point=0.019, Mesa Falls Tuff=0.008



Melt inclusion entrapment

Melt inclusions are trapped in crystals as they grow over time. Magmatic crystals trap primary inclusions as a result of some irregularity in growth conditions such as partial dissolution, rapid skeletal growth, or dendritic growth (e.g., Roedder 1979, 1984). The act of melt entrapment itself is not directly associated with any strain or stress on the surrounding host crystal. However, any subsequent changes in temperature that would produce differential volume changes (and thus a pressure differential) between the inclusion and host will produce elastic Eshelby-type stresses (“eigenstrain”) in the surrounding host (Eshelby 1957).

Depending on melt composition and volatile saturation at the time of entrapment, bubbles may be 1) co-entrapped with the melt (heterogeneous entrapment) or 2) may nucleate and grow after the melt parcel is trapped because of changes in solubility (pressure changes from melt-host differential thermal contraction). The presence and growth of bubbles in a melt parcel will change the inclusion’s bulk compressibility and thus its response to changes in stress, but we do not observe a clear difference in residual stress or misorientation between inclusions with and without bubbles (Figs. 4, 5, and 6).

Melt inclusion faceting

Melt inclusion faceting is a diffusion-limited process driven by surface free energy minimization. If the reduction in surface energy produced by the conversion of curved to flat surfaces (large to small Miller indices) is larger than the increase in total surface area (per volume) caused by the conversion from an ellipsoidal to polyhedral shape, inclusion faceting will spontaneously proceed (Roedder 1984). Because of these competing energy factors, it is possible that the observed semi-rounded polyhedrons of some melt inclusions here (e.g., Bishop, La Primavera, Huckleberry Ridge) are indeed their equilibrium shape (Wortis 1988). And because faceting is diffusion-dependent, appreciable

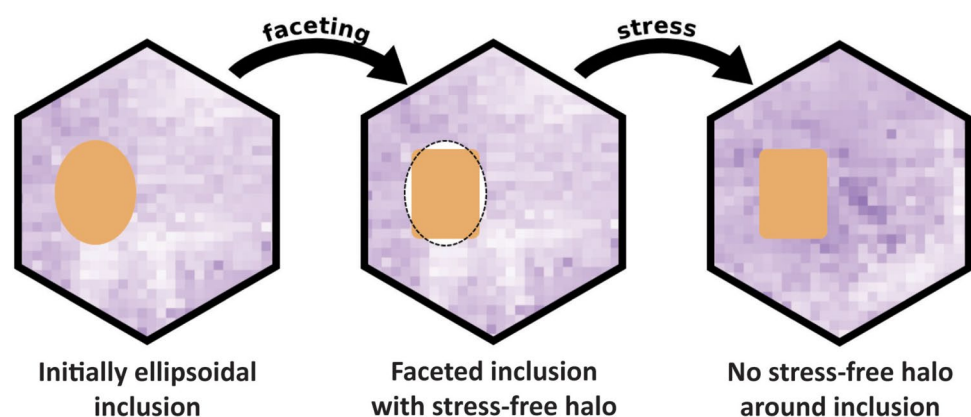
transport of Si atoms (in the case of quartz) is confined to high (near-magmatic) temperatures, with faceting ability steeply dropping off as the magma approaches the glass transition (Table 2) (Gualda et al. 2012). Using magmatic temperatures in Table 2, approximate faceting times calculated from inclusion radii are on the order of 10^2 – 10^3 years. These times represent the time from trapping an assumed ellipsoidal inclusion to a fully faceted inclusion, and thus reflect maximum timescales as equilibrium shapes could be rounded polyhedrons.

At the moment of reprecipitation during faceting, we assume the quartz around the inclusion to be stress-free (Fig. 10). Although some crystals do not show above-background stresses around inclusions (Bandelier, Huckleberry Ridge, Mesa Falls), we can infer that background stresses in all studied crystals were acquired post-faceting because of the lack of stress-free haloes around faceted inclusions (Fig. 5). Elevated stresses around Bishop, La Primavera, and Bluff Point inclusions follow the borders of the faceted inclusion shapes, also implying that these stresses were also imparted post-faceting. Because the faceting process can halt either due to energetical equilibrium being reached or a significant drop in temperature, the background stress and elevated stress (both elastic) near some inclusions can only be isolated to processes that operate sometime after inclusion faceting.

Fragmentation

As all studied crystals were extracted from tuffs, they have all experienced stresses associated with magma fragmentation. At critical strain rates required for fragmentation, the melt deforms elastically (Dingwell and Webb 1989; Gonnermann and Manga 2003; Caricchi et al. 2007). The mechanisms of brittle failure of the magma mixture can thus transmit large stresses to crystals immersed in the melt (Papale 1999). Median values of residual stresses in crystals studied here are 46–116 MPa, overlapping with experimentally-determined values for shear failure of

Fig. 10 Schematic representation of melt inclusion faceting process producing a stress-free halo in the reprecipitated quartz (white) proximal to the inclusion previously occupied by melt (orange). Crystals may be stressed before or during this process but are likely to at least experience a significant stress event after faceting (observed lack of low-stress halo around all inclusions, and elevated stress in some)



rhyolites ~ 100 MPa (Cordonnier et al. 2012; Wadsworth et al. 2018). We interpret fragmentation as the largest source of elastic deviatoric stress experienced by the quartz crystals from storage to deposition, and manifest as the overprinted background stresses distributed throughout the quartz ROIs (Fig. 5).

There are cracks in the quartz crystal around and through the La Primavera and Tuff of Bluff Point inclusions that do not reach the outside of each crystal. There is elevated elastic strain and stress, as well as plastic strain and presence of Dauphiné twins around the cracks in both samples (Figs. 3, 4, 5 and 6). Elevated stresses around inclusions and cracks are around 300–400 MPa, compared to background stresses (< 200 MPa) in most maps. We hypothesize that these cracks arose either from fragmentation stresses or the thermal volume change of the inclusion (discussed next). In either case, it is likely that stresses generated either outside or inside the crystal concentrated around the mechanical discontinuity (inclusion) in the crystal, especially around areas of high curvature. Although crystals can break during magma fragmentation (e.g., Cordonnier et al. 2012; van Zalinge et al. 2018; Taddeucci et al. 2021), the quartz crystals studied here did not. We understand these cracks as part of a time-integrated strain history that likely includes several events of overprinting as crystals grow and compact in the chamber and migrate towards the surface prior to and during fragmentation and eruption. Magmas can undergo multiple fracture and healing cycles while ascending in the conduit (Tuffen et al. 2003). On timescales relevant to magma ascent rates (minutes to several hours, Myers et al. 2018), crack annealing is possible and could limit the extent of observable cracks both in the photomicrographs and microstructural maps (Brantley et al. 1990).

Ascent and associated volume changes

As magma rises and cools, the quartz host and melt inclusion will thermally contract by slightly different amounts, which can produce Eshelby stresses in the crystal near the inclusion boundary (Fig. 11). Elevated stresses near inclusion boundaries that likely arose from this inclusion-host differential thermal contraction upon cooling appear in the Bishop, La Primavera, and Bluff Point residual stress maps, are extremely subtle in the Huckleberry and Mesa Falls maps, and are essentially absent in the Bandelier map (Fig. 5).

The precise physical impact of the faceted melt inclusion shape on crystal strain and stress distributions is not straightforward. Several models have been published that calculate the residual strain in isotropic and anisotropic hosts imparted by an anisotropic crystalline inclusion (e.g., Mazzucchelli et al. 2018; Gonzalez et al. 2021; Zhong et al. 2021). Although the elastic properties of melt inclusions

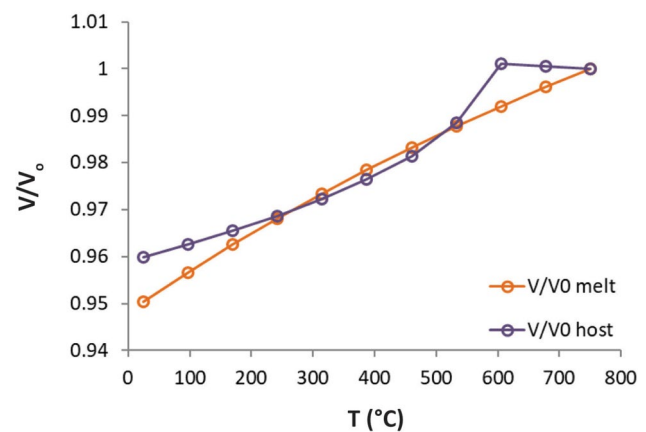


Fig. 11 Relative volume change of a typical rhyolitic melt inclusion in a quartz host from trapping (750 °C) to room temperature (25 °C). Thermal expansivity data for quartz from Kozu and Takane (1929) and for melt Lange and Carmichael (1990), Lange (1997), and Ochs and Lange (1997)

are isotropic, the challenge is how their particular degree of faceting (shape), position in the elastically anisotropic quartz lattice, and any internal features such as bubbles impact the surrounding stress magnitudes and distributions. To obtain an order of magnitude estimate of the induced strain (and stress) on the surrounding crystal during inclusion-host differential thermal contraction, we calculate the relative volume change of rhyolitic melt inclusions and quartz host from the inclusion trapping temperature (Table 2) to ambient temperature (25 °C). We compiled compositional data for each melt inclusion from the literature (Table 4). The volumetric data used for quartz were from Kozu and Takane (1929) and accounts for the α - β phase transition at 573 °C. The equations and thermal expansion data for major oxides in rhyolitic melt were obtained from Lange and Carmichael (1990), Lange (1997), and Ochs and Lange (1997). The calculations were performed in the Excel macro document from Moore et al. (2015).

For a melt inclusion trapped at 800 °C, the average relative volume change to surface temperatures is $V/V_{o_{MI}} = 0.9503$, and that of the quartz host $V/V_{o_{qtz}} = 0.9598$ (Fig. 11). The net volumetric strain is thus 9.5×10^{-3} (and -2.1×10^{-3} strain down to the average glass transition temperature ~ 420 °C). Using Hooke's Law and a Young's modulus of quartz $E \cong 94$ GPa (Ceccato et al. 2022), the maximum of inclusion-induced stress for this cooling range is ~ 893 MPa. Stress histograms all demonstrate some degree of positive skewness but the vast majority of stress values are under 200 MPa for all samples (Fig. 5). But several pixels per map do demonstrate values on the order of 700–900 MPa (Bishop Tuff) and 800–1000 MPa (La Primavera). Other maximum stress values, from only a few out of several thousand pixels per sample, are 990 MPa

Table 4 Melt inclusion (MI) compositions used to calculate glass transition temperatures and thus ΔT and consequent inclusion-host volume change strains

MI sample	SiO ₂	TiO ₂	Al ₂ O ₃	Fe ₂ O ₃	FeO	MnO	MgO	CaO	Na ₂ O	K ₂ O	H ₂ O	CO ₂	References
BT	78.6	–	11.8	–	0.63	–	0.04	0.43	3.02	5.33	3.77	0.0405	Anderson et al. (2000)
BaT	76.1	–	12.6	–	1.1	0.1	–	0.3	3.8	5.6	3.8	0.0054	Dunbar and Hervig (1992) Waelkens et al. (2022)
LP	73.76	0.16	11.33	0.79	1.01	0.05	0.05	0.22	3.77	4.74	4.13	–	Mahood (1981)
HRT	76.61	0.1	12.24	–	1.41	–	0.02	0.54	3.78	5.28	2.87	0.0276	Myers et al. (2016)
TBP	76.44	0.17	12.93	–	1.46	0.06	0.04	0.45	3.21	5.24	2.5	0.055	Christiansen (2001) Befus and Gardner (2016)
MFT	74.9	0.17	13.88	–	1.71	0.04	0.21	0.6	2.87	5.6	3.2	0.0308	Christiansen (2001) Tollan et al. (2019)

BT = Bishop Tuff, BaT = Bandelier Tuff, LP = La Primavera, HRT = Huckleberry Ridge Tuff, TBP = Tuff of Bluff Point, MFT = Mesa Falls Tuff

(Bandelier Tuff), 530 MPa (Tuff of Bluff Point), 250 MPa (Huckleberry Ridge Tuff), and 435 MPa (Mesa Falls Tuff). Although possible to impart, these magnitudes of residual stress are clearly not pervasive both proximal and distal to the inclusion-host boundaries.

It is unclear why some areas near inclusions preserve these elevated volume-change stresses and others do not, or less so, despite inclusions all being of similar size, shape, trapping temperatures, and ascent rates. Additionally, it is puzzling why quartz crystals preserve inconsistent orientations of strain (extension or compression) around the inclusions. For example, the strain around the Bishop inclusion is compressional while that of the top Tuff of Bluff Point inclusion is mostly extensional (Fig. 6). At this point (magma ascent), the crystal has undergone extensive plastic deformation in the mush and experienced large and sudden shear stresses upon fragmentation. Compounded with the inclusion shape and position effects, the distribution of these thermal stresses is also modulated by the spatiotemporally integrated strain history of each individual crystal. The state of twinning in the crystal and the interconnectivity and tortuosity of dislocation networks will certainly influence how these volume change stresses are recorded, whether by inhibiting their impact by plastic accommodation or recovery, or by locking them in before appreciable relaxation could take place. With the small sample number, it is not clear if the difference in orientation and magnitudes of volume change strain between samples are systematic, or would disappear at larger sample sizes.

Eruption and deposition

Befus et al. (2019) compared residual stress in volcanic quartz between different eruption styles and sizes, and found no elastic stresses associated with lava transport or pyroclastic surface processes. But all quartz crystals will still experience stresses during eruption, emplacement, and associated

cooling. One relevant process is the phase transition from hexagonal β -quartz to trigonal α -quartz at 573 °C, seen in the sharp volume change of quartz in Fig. 11. The Young's modulus of quartz changes its symmetry and sharply dips at 573 °C before recovering to a slightly lower value than high quartz (Ohno et al. 2006; Lakshtanov et al. 2007; Klumbach and Schilling 2017). The shift in quartz elastic moduli during eruption and cooling will impart more deviatoric strains in the crystal as slip systems become increasingly inactive as temperature drops. Yet this will also increase lattice friction and could promote mechanical twinning on planes with critical resolved shear stress. These mechanical twins can also be accompanied by transformational Dauphiné twinning (Wenk et al. 2009). Experiments on polycrystalline quartz by Wenk et al. (2007) found that Dauphiné twinning is highly temperature sensitive, and at 500 °C occurs at macroscopic differential stresses between 50 and 400 MPa. We cannot differentiate mechanical versus transformational Dauphiné twinning in our misorientation maps, but recognize that both varieties are likely to play a role in how strain was accommodated by each crystal. We attribute the various preserved amounts, morphologies, and distributions of Dauphiné twins observed in our samples to integrated elastic and plastic strain histories (such as lattice orientation and dislocation lock-up) of each crystal from the reservoir to Earth's surface.

Conclusion

Each crystal is understood to be a time-integrated, strain-compounded sample that offers a limited window into the true magnitude and extent of experienced stress and strain on its journey to the surface. There are many points in time and space when crystals are stressed. Deciphering that integrated history is challenging if not impossible. While the magnitudes of residual strain and stress in studied quartz crystals are similar, there is variation in the distribution and orientation of elastic strain and plasticity. There are too

many spatiotemporal mechanical and chemical processes that contribute to how crystals acquire and record lattice strain that these cannot be summed quantitatively to estimate a cumulative residual stress value for each crystal. Despite this, we can conclude that conditions in the magma reservoir such as viscous mush compaction can set up networks of dislocations that evolve over the crystal's lifetime and have a clear impact on how elastic and plastic deformation is accommodated and recorded by each crystal. Plastic deformation mechanisms modulate how elastic strains are preserved in the lattice, explaining the low magnitudes (~ 50–100 MPa medians) of observed residual stress compared to the strength of quartz (~ 10 GPa) (Fig. 7). We hypothesize that fragmentation is the largest source of elastic deviatoric stress preserved in quartz crystals and is responsible for the background stresses distributed throughout the imaged regions (Figs. 5 and 6).

Melt inclusion entrapment is a chronological signpost of when background stresses are imparted, and show how elastic Eshelby-type stresses can be recorded around faceted inclusion-host boundaries. In this way, even for inclusions that do not demonstrate these elevated stresses around their borders, the lack of stress-free haloes around inclusions shows that the majority of residual strains were imparted after faceting (Fig. 10). Finally, the magnitude of the recorded protracted strain histories of volcanic quartz is in some way ultimately limited by the capacity of the host. Further residual strain and stress studies on other early- and late-stage magmatic minerals (pyroxene, feldspars) would help inform whether the ~ 100 MPa order residual stresses are an authentic signal of magmatic stress, or more so an expression of the quartz host's mechanical properties. In any case, it is clear that quartz crystals preserve an incomplete record of the magnitude of strains experienced during their journey to Earth's surface.

Supplementary Information The online version contains supplementary material available at <https://doi.org/10.1007/s00410-024-02126-z>.

Acknowledgements We thank the editor Gordon Moore and reviewers George Bergantz and Andrew Cross for their thoughtful comments and useful suggestions. We extend our gratitude to Yao Li for his assistance in interpreting and visualizing the misorientation maps. This project was initially supported by the National Science Foundation grants NSF 1724429 and 1724469 and then by NSF 2042173. This project used beamline 12.3.2 of the Advanced Light Source at Lawrence Berkeley National Laboratory, funded under Department of Energy contract DE-AC02-05CH11231.

Author contributions All authors contributed to the study concept and design. Material preparation was performed by T. Cadena and K. Befus. Data collection was performed by N. Tamura and analysis was performed by T. Cadena and M. Manga. The first draft of the manuscript was written by T. Cadena and all authors commented on previous versions of the manuscript. All authors read and approved the final manuscript.

Funding This project was supported by National Science Foundation Grants NSF 1724429 and NSF 1724469, and Department of Energy contract DE-AC02-05CH11231.

Data availability Data collected at Laue microdiffraction beamline ALS 12.3.2, processed in X-ray Microdiffraction Analysis Software (XMAS) and (XtalCAMP), and used to make all microstructural maps presented in this study are available on Zenodo at <https://doi.org/10.5281/zenodo.8423439>.

Declarations

Conflict of interest The authors declare no relevant financial or non-financial interests.

Open Access This article is licensed under a Creative Commons Attribution 4.0 International License, which permits use, sharing, adaptation, distribution and reproduction in any medium or format, as long as you give appropriate credit to the original author(s) and the source, provide a link to the Creative Commons licence, and indicate if changes were made. The images or other third party material in this article are included in the article's Creative Commons licence, unless indicated otherwise in a credit line to the material. If material is not included in the article's Creative Commons licence and your intended use is not permitted by statutory regulation or exceeds the permitted use, you will need to obtain permission directly from the copyright holder. To view a copy of this licence, visit <http://creativecommons.org/licenses/by/4.0/>.

References

- Andersen N, Jicha B, Singer B, Hildreth W (2017) Incremental heating of Bishop Tuff sanidine reveals pre-eruptive radiogenic Ar and rapid remobilization from cold storage. *PNAS* 114:12407–12412. <https://doi.org/10.1073/pnas.1709581114>
- Anderson A, Davis A, Lu F (2000) Evolution of Bishop Tuff rhyolitic magma based on melt and magnetite inclusions and zoned phenocrysts. *J Petrol* 41:449–473. <https://doi.org/10.1093/ptrology/41.3.449>
- Audétat A, Schmitt A, Njul R, Saalfeld M, Borisova A, Lu Y (2023) New constraints on Ti diffusion in quartz and the priming of silicic volcanic eruptions. *Nat Commun* 14:4277. <https://doi.org/10.1038/s41467-023-39912-5>
- Bachmann O, Bergantz G (2004) On the origin of crystal-poor rhyolites: extracted from batholithic crystal mushes. *J Petrol* 45:1565–1582. <https://doi.org/10.1093/ptrology/egh019>
- Bachmann O, Huber C (2019) The inner workings of crustal distillation columns; the physical mechanisms and rates controlling phase separation in silicic magma reservoirs. *J Petrol* 60:3–18. <https://doi.org/10.1093/ptrology/egy103>
- Bailey R, Dalrymple GB, Lanphere M (1976) Volcanism, structure, and geochronology of Long Valley Caldera, Mono County California. *J Geophys Res* 81:725–744. <https://doi.org/10.1029/JB081i005p00725>
- Barabash R, Ice G (2005) Microdiffraction analysis of hierarchical dislocation organization. In: Buschow KH, Cahn R, Flemings M, Ilshner B, Kramer E, Mahajan S, Veyssi ere P (eds) *Encyclopedia of materials: science and technology*. Elsevier, pp 1–18. <https://doi.org/10.1016/B0-08-043152-6/02064-7>
- Barabash R, Ice G, Larson B, Yang W (2002) Application of white X-ray microbeams for the analysis of dislocation structures. *Rev Sci Instrum* 73(3):1652–1654. <https://doi.org/10.1063/1.1445830>

- Barbee O, Chesner C, Deering C (2020) Quartz crystals in Toba rhyolites show textures symptomatic of rapid crystallization. *Am Min* 105:194–226. <https://doi.org/10.2138/am-2020-6947>
- Barboni M, Boehnke P, Schmitt A, Baumgartner L (2016) Warm storage for arc magmas. *PNAS* 113:13959–13964. <https://doi.org/10.1073/pnas.1616129113>
- Befus K, Gardner J (2016) Magma storage and evolution of the most recent effusive and explosive eruptions from Yellowstone Caldera. *Contrib Mineral Petrol* 171:30. <https://doi.org/10.1007/s00410-016-1244-x>
- Befus K, Manga M, Stan C, Tamura N (2019) Volcanoes erupt stressed quartz crystals. *Geophys Res Lett* 46:8791–8800. <https://doi.org/10.1029/2019GL083619>
- Befus K, Ruefer A, Allison C, Thompson J (2023) Quartz-hosted inclusions and embayments reveal storage, fluxing, and ascent of the Mesa Falls Tuff Yellowstone. *EPSL* 601:117909. <https://doi.org/10.1016/j.epsl.2022.117909>
- Bergantz G, Schleicher J, Burgisser A (2017) On the kinematics and dynamics of crystal-rich systems. *J Geophys Res Solid Earth* 122:6131–6159. <https://doi.org/10.1002/2017JB014218>
- Boro J, Wolff J, Neill O, Steiner A, Ramos F (2021) Titanium diffusion profiles and melt inclusion chemistry and morphology in quartz from the Tshirege Member of the Bandelier Tuff. *Am Min* 106:620–632. <https://doi.org/10.2138/am-2021-7395>
- Bragg WH, Bragg WL (1913) The reflexion of X-rays by crystals. *Proc R Soc Lond A* 88:428–438. <https://doi.org/10.1098/rspa.1913.0040>
- Brantley S, Evans B, Hickman S, Crerar D (1990) Healing of microcracks in quartz: implications for fluid flow. *Geology* 18:136–139. [https://doi.org/10.1130/0091-7613\(1990\)018%3c0136:HOM-IQI%3e2.3.CO;2](https://doi.org/10.1130/0091-7613(1990)018%3c0136:HOM-IQI%3e2.3.CO;2)
- Brewer L, Othon M, Young L, Angelu T (2006) Misorientation mapping for visualization of plastic deformation via electron backscattered diffraction. *Microsc Microanal* 12:85–91. <https://doi.org/10.1017/S1431927606060120>
- Broz ME, Cook RF, Whitney DL (2006) Microhardness, toughness, and modulus of Mohs scale minerals. *Am Min* 91:135–142. <https://doi.org/10.2138/am.2006.1844>
- Budiman A, Narayanan K, Li N, Wang J, Tamura N, Kunz M, Misra A (2015) Plasticity evolution in nanoscale Cu/Nb single-crystal multilayers as revealed by synchrotron X-ray microdiffraction. *Mater Sci Eng A* 635:6–12. <https://doi.org/10.1016/j.msea.2015.03.067>
- Caricchi L, Burlini L, Ulmer P, Gerya T, Vassalli M, Papale P (2007) Non-Newtonian rheology of crystal-bearing magmas and implications for magma ascent dynamics. *EPSL* 264:402–419. <https://doi.org/10.1016/j.epsl.2007.09.032>
- Cassidy M, Manga M, Cashman K et al (2018) Controls on explosive-effusive volcanic eruption styles. *Nat Commun* 9:2839. <https://doi.org/10.1038/s41467-018-05293-3>
- Cates ME, Wittmer JP, Bouchaud JP, Claudin P (1998) Jamming, force chains, and fragile matter. *PRL* 81:1841–1844. <https://doi.org/10.1103/PhysRevLett.81.1841>
- Catti M (1985) Calculation of elastic constants by the method of crystal static deformation. *Acta Cryst A* 41:494–500. <https://doi.org/10.1107/S0108767385001052>
- Ceccato A, Menegon L, Hansen L (2022) Strength of dry and wet quartz in the low-temperature plasticity regime: insights from nanoindentation. *Geophys Res Lett* 49:e2021GL094633. <https://doi.org/10.1029/2021GL094633>
- Chen K, Kunz M, Tamura N, Wenk HR (2015) Residual stress preserved in quartz from the San Andreas Fault Observatory at Depth. *Geology* 43:219–222. <https://doi.org/10.1130/G36443.1>
- Christensen JN, Halliday AN (1996) Rb-Sr ages and Nd isotopic compositions of melt inclusions from the Bishop Tuff and the generation of silicic magma. *EPSL* 144:547–561. [https://doi.org/10.1016/S0012-821X\(96\)00181-1](https://doi.org/10.1016/S0012-821X(96)00181-1)
- Christiansen RL, Lowenstern JB, Smith RB, Heasler H, Morgan LA, Nathansen M, Mastin LG, Muffler LJP, Robinson JE (2007) Preliminary assessment of volcanic and hydrothermal hazards in Yellowstone National Park and vicinity. USGS Open-File Report 2007–1071:94. <https://doi.org/10.3133/ofr20071071>
- Christiansen RL (2001) Geology of yellowstone national park: the quaternary and Pliocene Yellowstone Plateau Volcanic Field of Wyoming, Idaho, and Montana. USGS Professional Paper 729-G. <https://doi.org/10.3133/pp729G>
- Chung JS, Ice G (1999) Automated indexing for texture and strain measurement with broad-bandpass xray microbeams. *J Appl Phys* 86:5249–5255. <https://doi.org/10.1063/1.371507>
- Cooper K (2019) Time scales and temperatures of crystal storage in magma reservoirs: implications for magma reservoir dynamics. *Phil Trans R Soc A* 377:20180009. <https://doi.org/10.1098/rsta.2018.0009>
- Cordonnier B, Caricchi L, Pistone M, Castro J, Hess KU, Gottschaller S, Manga M, Dingwell DB, Burlini L (2012) The viscous brittle transition of crystal-bearing silicic melt: direct observation of magma rupture and healing. *Geology* 40:611–614. <https://doi.org/10.1130/G3914.1>
- Costa F (2008) Chapter 1: Residence times of silicic magmas associated with calderas. In: Gottsmann J, Martí J (eds) *Developments in volcanology*, vol 10. Elsevier, pp 1–55. [https://doi.org/10.1016/S1871-644X\(07\)00001-0](https://doi.org/10.1016/S1871-644X(07)00001-0)
- Crowley JL, Schoene B, Bowring SA (2007) U–Pb dating of zircon in the Bishop Tuff at the millennial scale. *Geology* 35:1123–1126. <https://doi.org/10.1130/G24017A.1>
- Dingwell DB, Webb SL (1989) Structural relaxation in silicate melts and non-Newtonian melt rheology in geologic processes. *Phys Chem Miner* 16:508–516. <https://doi.org/10.1007/BF00197020>
- Dunbar N, Hervig R (1992) Volatile and trace element composition of melt inclusions from the Lower Bandelier Tuff: Implications for magma chamber processes and eruptive style. *J Geophys Res Solid Earth* 97:15151–15170. <https://doi.org/10.1029/92JB01340>
- Eshelby JD (1957) The determination of the elastic field of an ellipsoidal inclusion, and related problems. *Proc R Soc Lond A* 241:376–396. <https://doi.org/10.1098/rspa.1957.0133>
- Friedrich W, Knipping P, Laue M (1912) Interferenz-Erscheinungen bei Röntgenstrahlen. In: *Sitzungsberichte der Königlich Bayerischen Akademie der Wissenschaften, Math. Phys. Klasse* 303–322. Verl. d. Königl. Bayer
- Frondel C (1962) *The system of mineralogy of James Dwight Dana and Edward Salisbury Dana, vol III: silica minerals*. Wiley
- Giordano D, Russell J, Dingwell D (2008) Viscosity of magmatic liquids: a model. *EPSL* 271:123–134. <https://doi.org/10.1016/j.epsl.2008.03.038>
- Goldsby DL, Rar A, Pharr GM, Tullis TE (2004) Nanoindentation creep of quartz, with implications for rate- and state-variable friction laws relevant to earthquake mechanics. *JMR* 19:357–365. [https://doi.org/10.1016/0040-1951\(83\)90266-4](https://doi.org/10.1016/0040-1951(83)90266-4)
- Gonnermann H, Manga M (2003) Explosive volcanism may not be an inevitable consequence of magma fragmentation. *Nature* 426:432–435. <https://doi.org/10.1038/nature02138>
- Gonzalez JP, Mazzucchelli ML, Angel RJ, Alvaro M (2021) Elastic geobarometry for anisotropic inclusions in anisotropic host minerals: quartz-in-zircon. *J Geophys Res Solid Earth* 126:e2021JB022080. <https://doi.org/10.1029/2021JB022080>
- Gualda G, Pamukcu A, Ghiorsio M, Anderson A Jr, Sutton S, Rivers M (2012) Timescale of quartz crystallization and the longevity of the Bishop Giant Magma Body. *PLoS ONE* 7:e37492. <https://doi.org/10.1371/journal.pone.0037492>

- Gualda G, Gravley D, Deering C, Ghiorso M (2019) Magma extraction pressures and the architecture of volcanic plumbing systems. *EPSL* 522:118–124. <https://doi.org/10.1016/j.epsl.2019.06.020>
- Heaney PJ, Veblen DR (1991) Observation of the α - β phase transition in quartz: a review of imaging and diffraction studies and some new results. *Am Min* 76:1018–1032
- Hervig RL, Dunbar NW (1992) Cause of chemical zoning in the Bishop (California) and Bandelier (New Mexico) magma chambers. *EPSL* 111:97–108. [https://doi.org/10.1016/0012-821X\(92\)90172-R](https://doi.org/10.1016/0012-821X(92)90172-R)
- Holness MB (2018) Melt segregation from silicic crystal mushes: a critical appraisal of possible mechanisms and their microstructural record. *Contrib Mineral Petrol* 173:48. <https://doi.org/10.1007/s00410-018-1465-2>
- Holness MB, Vukmanovic Z, Mariani E (2017) Assessing the role of compaction in the formation of adcumulates: a microstructural perspective. *J Petrol* 58:643–673. <https://doi.org/10.1093/ptrology/egx037>
- Hughes D, Hansen N, Bammann D (2003) Geometrically necessary boundaries, incidental dislocation boundaries and geometrically necessary dislocations. *Scr Mater* 48:147–153. [https://doi.org/10.1016/S1359-6462\(02\)00358-5](https://doi.org/10.1016/S1359-6462(02)00358-5)
- Ice G, Chung J, Lowe W, Williams E, Edelman J (2000) Small displacement monochromator for microdiffraction experiments. *Rev Sci Instrum* 71:2001–2006. <https://doi.org/10.1063/1.1150568>
- Kendrick JE, Lavallée Y, Mariani E et al (2017) Crystal plasticity as an indicator of the viscous-brittle transition in magmas. *Nat Commun* 8:1926. <https://doi.org/10.1038/s41467-017-01931-4>
- Klumbach S, Schilling FR (2017) Anisotropic viscoelastic properties of quartz and quartzite in the vicinity of the α - β phase transition. *Phys Chem Miner* 44:627–637. <https://doi.org/10.1007/s00269-017-0888-z>
- Kozu S, Takane K (1929) Influence of temperature on the axial ratio, the interfacial angle, and the volume of quartz. *Sci Reports of Tohoku Imp. Univ., Series III* 2:204–208. <https://doi.org/10.2465/ganko1929.1.103>
- Kunz M, Chen K, Tamura N, Wenk HR (2009) Evidence for residual elastic strain in deformed natural quartz. *Am Min* 94:1059–1062. <https://doi.org/10.2138/am.2009.3216>
- Lakshatanov DL, Sinogeikin SV, Bass JD (2007) High-temperature phase transitions and elasticity of silica polymorphs. *Phys Chem Miner* 34:11–22. <https://doi.org/10.1007/s00269-006-0113-y>
- Lange R (1997) A revised model for the density and thermal expansivity of K_2Na_2O - CaO - MgO - Al_2O_3 - SiO_2 -liquids from 700–1900 K: extension to crustal magmatic temperatures. *Contrib Mineral Petrol* 130:1–11. <https://doi.org/10.1007/s004100050345>
- Lange R, Carmichael I (1990) Thermodynamic properties of silicate liquids with emphasis on density, thermal expansion, and compressibility. *Rev Mineral Geochem* 24:25–59. <https://doi.org/10.1515/9781501508769-006>
- Lanphere MA, Champion DE, Christiansen RL, Izett GA, Obradovich JD (2002) Revised ages for tuffs of the Yellowstone Plateau volcanic field; assignment of the Huckleberry Ridge Tuff to a new geomagnetic polarity event. *GSA Bull* 114:559–568. [https://doi.org/10.1130/0016-7606\(2002\)114%3c0559:RAFTOT%3e2.0.CO;2](https://doi.org/10.1130/0016-7606(2002)114%3c0559:RAFTOT%3e2.0.CO;2)
- Lavallée Y, Kendrick J (2022) Strain localization in magmas. *Rev Mineral Geochem* 87:721–765. <https://doi.org/10.2138/rmg.2022.87.15>
- Li Y, Wan L, Chen K (2015) A look-up table based approach to characterize crystal twinning for synchrotron X-ray Laue microdiffraction scans. *J Appl Cryst* 48:747–757. <https://doi.org/10.1107/S1600576715004896>
- Li Y, Chen K, Dang X, Zhang F, Tamura N, Ku CS, Kang H, Wenk HR (2020) XtalCAMP: a comprehensive program for the analysis and visualization of scanning Laue X-ray micro-/nanodiffraction data. *J Appl Cryst* 53:1392–1403. <https://doi.org/10.1107/S1600576720010882>
- Magid K, Lilleodden E, Tamura N, Florando J, Lassila D, LeBlanc M, Barabash R, Morris, Jr. J (2004) X-ray microdiffraction characterization of deformation heterogeneities in BCC crystals. In: *Materials Research Society Symposium Proceedings*, 840:Q7.2.1–6. <https://doi.org/10.1557/PROC-840-Q7.2>
- Magid K, Florando J, Lassila D, LeBlanc M, Tamura N, Morris J Jr (2009) Mapping mesoscale heterogeneity in the plastic deformation of a copper single crystal. *Philos Mag* 89:77–107. <https://doi.org/10.1080/14786430802558577>
- Mahood G (1981) A summary of the geology and petrology of the Sierra La Primavera, Jalisco Mexico. *J Geophys Res* 86:10137–10152. <https://doi.org/10.1029/JB086iB11p10137>
- Mazzucchelli M, Burnley P, Angel R, Morganti S, Domeneghetti M, Nestola F, Alvaro M (2018) Elastic geothermobarometry: corrections for the geometry of the host-inclusion system. *Geology* 46:231–234. <https://doi.org/10.1130/G39807.1>
- McLellan AG (1978) The thermodynamic theory of the growth of Dauphiné twinning in quartz under stress. *J Phys c: Solid State Phys* 11:4665. <https://doi.org/10.1088/0022-3719/11/23/013>
- Menegon L, Piazzolo S, Pennacchioni G (2011) The effect of Dauphiné twinning on plastic strain in quartz. *Contrib Mineral Petrol* 161:635–652. <https://doi.org/10.1007/s00410-010-0554-7>
- Moffat K (2019) Laue diffraction and time-resolved crystallography: a personal history. *Phil Trans R Soc A* 377:20180243. <https://doi.org/10.1098/rsta.2018.0243>
- Moore LR, Gazel E, Tuohy R, Lloyd AS, Esposito R, Steele-MacInnis M, Hauri EH, Wallace PJ, Plank T, Bodnar RJ (2015) Bubbles matter: an assessment of the contribution of vapor bubbles to melt inclusion volatile budgets. *Am Min* 100:806–823. <https://doi.org/10.2138/am2015-5036>
- Myers M, Wallace P, Wilson C, Morter B, Swallow E (2016) Prolonged ascent and episodic venting of discrete magma batches at the onset of the Huckleberry Ridge supereruption, Yellowstone. *EPSL* 451:285–297. <https://doi.org/10.1016/j.epsl.2016.07.023>
- Myers M, Wallace P, Wilson C, Watkins J, Liu Y (2018) Ascent rates of rhyolitic magma at the onset of three caldera-forming eruptions. *Am Min* 103:952–965. <https://doi.org/10.2138/am-2018-6225>
- Noyan I, Cohen J (1987) Residual stress: measurement by diffraction and interpretation. Springer-Verlag, pp 13–46. ISBN: 978-1-4613-9571-3
- Ochs F III, Lange R (1997) The partial molar volume, thermal expansivity, and compressibility of H₂O in NaAlSi₃O₈ liquid: new measurements and an internally-consistent model. *Contrib Mineral Petrol* 129:155–165. <https://doi.org/10.1007/s004100050329>
- Ohno I, Harada K, Yoshitomi C (2006) Temperature variation of elastic constants of quartz across the α - β transition. *Phys Chem Miner* 33:1–9. <https://doi.org/10.1007/s00269-005-0008-3>
- Pamukcu A, Gualda G, Anderson A Jr (2012) Crystallization stages of the Bishop Tuff Magma body recorded in crystal textures in pumice clasts. *J Petrol* 53:589–609. <https://doi.org/10.1093/ptrology/egr072>
- Pamukcu A, Gualda G, Begue F, Gravley D (2015) Melt inclusion shapes: timekeepers of short-lived giant magma bodies. *Geology* 43:947–950. <https://doi.org/10.1130/G37021.1>
- Papale P (1999) Strain-induced magma fragmentation in explosive eruptions. *Nature* 397:425–428. <https://doi.org/10.1038/17109>
- Phillips GF, Kyle PR, McIntosh WC, Dunbar NW, Gardner JN (2007) The 40Ar/39Ar age constraints on the duration of resurgence at the Valles caldera, New Mexico. *J Geophys Res Solid Earth* 112(B8):B08201. <https://doi.org/10.1029/2006JB004511>
- Piazzolo S, Prior DJ, Holness MD (2005) The use of combined cathodoluminescence and EBSD analysis: a case study investigating grain boundary migration mechanisms in quartz. *J Microsc* 217:152–161. <https://doi.org/10.1111/j.1365-2818.2005.01423.x>

- Poshadel A, Dawson P, Johnson G (2012) Assessment of deviatoric lattice strain uncertainty for polychromatic X-ray microdiffraction experiments. *J Synchrotron Rad* 19:237–244. <https://doi.org/10.1107/S0909049511050400>
- Reid MR, Coath CD (2000) In situ U–Pb ages of zircons from the Bishop Tuff: no evidence for long crystal residence times. *Geology* 28:443–446. [https://doi.org/10.1130/0091-7613\(2000\)28%3c443:ISUAOZ%3e2.0.CO;2](https://doi.org/10.1130/0091-7613(2000)28%3c443:ISUAOZ%3e2.0.CO;2)
- Rivera T, Schmitz M, Jicha B, Crowley J (2016) Zircon petrology and ⁴⁰Ar/³⁹Ar sanidine dates for the mesa falls tuff: crystal-scale records of magmatic evolution and the short lifespan of a large Yellowstone Magma Chamber. *J Petrol* 57:1677–1704. <https://doi.org/10.1093/petrology/egw053>
- Robach O, Micha JS, Ulrich O, Gergaud P (2011) Full local elastic strain tensor from Laue microdiffraction: simultaneous Laue pattern and spot energy measurement. *J Appl Cryst* 44:688–696. <https://doi.org/10.1107/S002188981102320X>
- Roedder E (1979) Origin and significance of magmatic inclusions. *Bull Minéral* 102:5–6. <https://doi.org/10.3406/bulmi.1979.7299>
- Roedder E (1984) Fluid inclusions. Reviews in mineralogy 12. De Gruyter. <https://doi.org/10.1515/9781501508271>
- Rubin A, Cooper K, Till C, Kent A, Costa F et al (2017) Rapid cooling and cold storage in a silicic magma reservoir recorded in individual crystals. *Science* 356:1154–1156. <https://doi.org/10.1126/science.aam8720>
- Saalfeld M, Myers M, deGraffenried R, Shea T, Waelkens C (2022) On the rise: using reentrants to extract magma ascent rates in the Bandelier Tuff caldera complex, New Mexico, USA. *Bull Volcanol* 84:4. <https://doi.org/10.1007/s00445-021-01518-4>
- Schindelin J, Arganda-Carreras I, Frise E et al (2012) Fiji: an open-source platform for biological-image analysis. *Nat Methods* 9:676–682. <https://doi.org/10.1038/nmeth.2019>
- Seitz S, Pultitz B, Baumgartner L, Escrig S, Meibom A, Bouvier AS (2016) Short magmatic residence times of quartz phenocrysts in Patagonian rhyolites associated with Gondwana breakup. *Geology* 44:67–70. <https://doi.org/10.1130/G37232.1>
- Seropian G, Rust A, Sparks S (2018) The gravitational stability of lenses in magma mushes: confined Rayleigh–Taylor instabilities. *J Geophys Res Solid Earth* 123:3593–3607. <https://doi.org/10.1029/2018JB015523>
- Smith R, Bailey R (1966) The Bandelier Tuff: a study of ash-flow eruption cycles from zoned magma chambers. *Bull Volcanol* 29:83–103. <https://doi.org/10.1007/BF02597146>
- Sosa-Ceballos G (2015) The Tala Tuff, La Primavera caldera Mexico. Pre-eruptive conditions and magma processes before eruption. In: 2015 AGU Fall meeting abstracts, San Francisco. V43B-3115. <https://ui.adsabs.harvard.edu/abs/2015AGUFM.V43B3115>
- Sourisseau D, Arce J, Macías J, Sosa Ceballos G, García Tenorio F, Avellán D, Saucedo-Girón R et al (2023) Genesis and evolution of the post-caldera pyroclastic rhyolites from La Primavera caldera, Jalisco, Mexico: a crystal mush perspective. *J Volcanol Geotherm Res* 442:107911. <https://doi.org/10.1016/j.jvolgeores.2023.107911>
- Straumanis ME (1949) The precision determination of lattice constants by the powder and rotating crystal methods and applications. *J Appl Phys* 20:726–734. <https://doi.org/10.1063/1.1698520>
- Strozewski B, Sly M, Flores K, Skemer P (2021) Viscoplastic rheology of α -quartz investigated by nanoindentation. *J Geophys Res Solid Earth* 126:e2021JB022229. <https://doi.org/10.1029/2021JB022229>
- Swallow E, Wilson C, Charlier B, Gamble J (2019) The Huckleberry Ridge Tuff, Yellowstone: evacuation of multiple magmatic systems in a complex episodic eruption. *J Petrol* 60:1371–1426. <https://doi.org/10.1093/petrology/egz034>
- Taddeucci J, Cimarelli C, Alatorre-Ibargüengoitia MA et al (2021) Fracturing and healing of basaltic magmas during explosive volcanic eruptions. *Nat Geosci* 14:248–254. <https://doi.org/10.1038/s41561-021-00708-1>
- Tamura N (2014) XMAS: a versatile tool for analyzing synchrotron X-ray microdiffraction data, strain and dislocation gradients from diffraction. In: Barabash R, Ice G (eds) strain and dislocation gradients from diffraction. Imperial College Press, pp 125–155. https://doi.org/10.1142/9781908979636_0004
- Tamura N, MacDowell AA, Spolenak R, Valek BC, Bravman JC, Brown WL, Celestre RS, Padmore HA, Batterman BW, Patel JR (2003) Scanning X-ray microdiffraction with submicron white beam for strain/stress and orientation mapping in thin films. *J Synchrotron Rad* 10:137–143. <https://doi.org/10.1107/S0909049502021362>
- Tamura N, Kunz M, Chen K, Celestre RS, MacDowell AA, Warwick T (2009) A superbend X-ray microdiffraction beamline at the advanced light source. *Mater Sci Eng A* 524:28–32. <https://doi.org/10.1016/j.msea.2009.03.062>
- Tollan P, Ellis B, Troch J et al (2019) Assessing magmatic volatile equilibria through FTIR spectroscopy of unexposed melt inclusions and their host quartz: a new technique and application to the Mesa Falls Tuff Yellowstone. *Contrib Mineral Petrol* 174:24. <https://doi.org/10.1007/s00410-019-1561-y>
- Tuffen H, Dingwell DB, Pinkerton H (2003) Repeated fracture and healing of silicic magma generates flow banding and earthquakes? *Geology* 31:1089–1092. <https://doi.org/10.1130/G19777.1>
- Tullis J, Tullis T (1972) Preferred orientation of quartz produced by mechanical Dauphiné twinning: thermodynamics and axial experiments. In: Heard HC, Borg IY, Carter NI, Raleigh CB (eds) Flow and fracture of rocks, geophysical monograph, vol 16. American Geophysical Union, pp 67–82. <https://doi.org/10.1029/GM016p0067>
- van den Bogaard P, Schirnick C (1995) ⁴⁰Ar/³⁹Ar laser probe ages of Bishop Tuff quartz phenocrysts substantiate long-lived silicic magma chamber at Long Valley, United States. *Geology* 23:759–762. [https://doi.org/10.1130/0091-7613\(1995\)023%3c0759:AALPAO%3e2.3.CO;2](https://doi.org/10.1130/0091-7613(1995)023%3c0759:AALPAO%3e2.3.CO;2)
- Van Tendeloo G, Van Landuyt J, Amelickx S (1976) The α – β phase transition in quartz and AlPO₄ as studied by electron microscopy and diffraction. *Phys Status Solidi A* 33:723–735. <https://doi.org/10.1002/pssa.2210330233>
- van Zalinge ME, Cashman KV, Sparks RSJ (2018) Causes of fragmented crystals in ignimbrites: a case study of the Cardones ignimbrite Northern Chile. *Bull Volcanol* 80:22. <https://doi.org/10.1007/s00445-018-1196-2>
- van Zalinge ME, Mark D, Sparks S, Tremblay M, Keller C, Cooper F, Rust A (2022) Timescales for pluton growth, magma-chamber formation and super-eruptions. *Nature* 608:87–92. <https://doi.org/10.1038/s41586-022-04921-9>
- Vinet N, Molina P, Flemming R, Houde V, Morgado E, Barra F, Morata D (2015) Quantification and origin of intracrystalline deformation of olivine from basalts of the Andean Southern volcanic zone: a multidisciplinary study. In: Congreso Geologica Chileno XIV 476–479
- Wadsworth FB, Witcher T, Vossen CE, Hess KU, Unwin HE, Scheu B, Castro JM, Dingwell DB (2018) Combined effusive-explosive silicic volcanism straddles the multiphase viscous-to-brittle transition. *Nat Commun* 9:4696. <https://doi.org/10.1038/s41467-018-07187-w>
- Waelkens CM, Stix J, Eves E, Gonzalez C, Martineau D (2022) H₂O and CO₂ evolution in the Bandelier Tuff sequence reveals multiple and discrete magma replenishments. *Contrib Mineral Petrol* 177:1–23. <https://doi.org/10.1007/s00410-021-01866-6>

- Wallace P, Kendrick J, Miwa T, Ashworth J, Coats R, Utley J et al (2019) Petrological architecture of a magmatic shear zone: a multidisciplinary investigation of strain localisation during magma ascent at Unzen Volcano, Japan. *J Petrol* 60:791–826. <https://doi.org/10.1093/petrology/egz016>
- Warren BE (1959) X-ray studies of deformed metals. *Prog Met Phys* 8:147–202. [https://doi.org/10.1016/0502-8205\(59\)90015-2](https://doi.org/10.1016/0502-8205(59)90015-2)
- Warren BE, Averbach BL (1950) The effect of coldwork distortion on X-ray patterns. *J Appl Phys* 21:595–599. <https://doi.org/10.1063/1.1699713>
- Watts K, Bindeman I, Schmitt A (2012) Crystal scale anatomy of a dying supervolcano: an isotope and geochronology study of individual phenocrysts from voluminous rhyolites of the Yellowstone caldera. *Contrib Mineral Petrol* 164:45–67. <https://doi.org/10.1063/1.1699713>
- Wenk HR, Bortolotti M, Barton N, Oliver E, Brown D (2007) Dauphiné twinning and texture memory in polycrystalline quartz. Part 2: in situ neutron diffraction compression experiments. *Phys Chem Miner* 34:599–607. <https://doi.org/10.1007/s00269-007-0174-6>
- Wenk HR, Barton N, Bortolotti M, Vogel S, Voltolini M, Lloyd G, Gonzalez G (2009) Dauphiné twinning and texture memory in polycrystalline quartz. Part 3: texture memory during phase transformation. *Phys Chem Miner* 36:567–583. <https://doi.org/10.1007/s00269-009-0302-6>
- Wenk HR, Chandler BC, Chen K, Li Y, Tamura N, Yu R (2020) Residual lattice strain in quartzites as a potential palaeo-piezometer. *Geophys J Int* 222:1363–1378. <https://doi.org/10.1093/gji/ggaa226>
- Wheeler J, Prior D, Jiang Z et al (2001) The petrological significance of misorientations between grains. *Contrib Mineral Petrol* 141:109–124. <https://doi.org/10.1007/s004100000225>
- Whitney DL, Broz M, Cook RF (2007) Hardness, toughness, and modulus of some common metamorphic minerals. *Am Min* 92:281–288. <https://doi.org/10.2138/am.2007.2212>
- Wieser PE, Edmonds M, Maclennan J, Wheeler J (2020) Microstructural constraints on magmatic mushes under Kilauea Volcano Hawai'i. *Nat Commun* 11:14. <https://doi.org/10.1038/s41467-019-13635-y>
- Wilkinson AJ, Tarleton E, Vilalta-Clemente A, Jiang J, Britton TB, Collins DM (2014) Measurement of probability distributions for internal stresses in dislocated crystals. *Appl Phys Lett* 105:181907. <https://doi.org/10.1063/1.4901219>
- Winick JA, McIntosh WC, Dunbar NW (2001) Melt-inclusion-hosted excess ⁴⁰Ar in quartz crystals of the Bishop and Bandelier magma systems. *Geology* 29:275–278. [https://doi.org/10.1130/0091-7613\(2001\)029%3c0275:MIHEAI%3e2.0.CO;2](https://doi.org/10.1130/0091-7613(2001)029%3c0275:MIHEAI%3e2.0.CO;2)
- Wortis M (1988) Equilibrium crystal shapes and interfacial phase transitions. In: Vanselow R, Howe R (eds) *Chemistry and physics of solid surfaces VII*, Springer Series in Surface Sciences, vol 10. Springer, pp 367–405. https://doi.org/10.1007/978-3-642-73902-6_13
- Zhao Y, Zhang J (2008) Microstrain and grain-size analysis from diffraction peak width and graphical derivation of high-pressure thermomechanics. *J Appl Cryst* 41:1095–1108. <https://doi.org/10.1107/S0021889808031762>
- Zhong X, Dabrowski M, Jamtveit B (2021) Analytical solution for residual stress and strain preserved in anisotropic inclusion entrapped in an isotropic host. *Solid Earth* 12:817–833. <https://doi.org/10.5194/se-12-817-2021>
- Zhou G, Zhu W, Shen H et al (2016) Real-time microstructure imaging by Laue microdiffraction: a sample application in laser 3D printed Ni-based superalloys. *Sci Rep* 6:28144. <https://doi.org/10.1038/srep28144>

Publisher's Note Springer Nature remains neutral with regard to jurisdictional claims in published maps and institutional affiliations.